minerals

MDPI

Article

Lithium-, Phosphorus-, and Fluorine-Rich Intrusions and the Phosphate Sequence at Segura (Portugal): A Comparison with Other Hyper-Differentiated Magmas

Michel Cathelineau [1,*], Marie-Christine Boiron [1], Andreï Lecomte [1], Ivo Martins [2], Ícaro Dias da Silva [2] and Antonio Mateus [2]

[1] Université de Lorraine, CNRS, GeoRessources, 54000 Nancy, France; marie-christine.boiron@univ-lorraine.fr (M.-C.B.); andrei.lecomte@univ-lorraine.fr (A.L.)
[2] Faculdade de Ciências, Instituto Dom Luiz, Universidade de Lisboa, Campo Grande, 1749-016 Lisboa, Portugal; ivojmartins@gmail.com (I.M.); ifsilva@fc.ul.pt (Í.D.S.); amateus@ciencias.ulisboa.pt (A.M.)
* Correspondence: michel.cathelineau@univ-lorraine.fr

Abstract: Near the Segura pluton, hyper-differentiated magmas enriched in F, P, and Li migrated through shallowly dipping fractures, which were sub-perpendicular to the schistosity of the host Neoproterozoic to Lower Cambrian metasedimentary series, to form two swarms of low-plunging aplite–pegmatite dykes. The high enrichment factors for the fluxing elements (F, P, and Li) compared with peraluminous granites are of the order of 1.5 to 5 and are a consequence of the extraction of low-viscosity magma from the crystallising melt. With magmatic differentiation, increased P and Li activity yielded the crystallisation of the primary amblygonite–montebrasite series and Fe-Mn phosphates. The high activity of sodium during the formation of the albite–topaz assemblage in pegmatites led to the replacement of the primary phosphates by lacroixite. The influx of external, post-magmatic, and Ca-Sr-rich hydrothermal fluids replaced the initial Li-Na phosphates with phosphates of the goyazite–crandallite series and was followed by apatite formation. Dyke emplacement in metasediments took place nearby the main injection site of the muscovite granite, which plausibly occurred during a late major compression event.

Keywords: peraluminous aplite and pegmatite; phosphorus; lithium; fluorine; eosphorite; montebrasite; Raman spectroscopy

Citation: Cathelineau, M.; Boiron, M.-C. ; Lecomte, A. ; Martins, I. ; Dias da Silva, I.; Mateus, A. Lithium-, Phosphorus-, and Fluorine-Rich Intrusions and the Phosphate Sequence at Segura (Portugal): A Comparison with Other Hyper-Differentiated Magmas. *Minerals* **2024**, *14*, 287. https://doi.org/10.3390/min14030287

Academic Editor: Ignez de Pinho Guimarães

Received: 25 January 2024
Revised: 19 February 2024
Accepted: 4 March 2024
Published: 8 March 2024

1. Introduction

Lithium- and phosphorus-rich pegmatites are often evidence of the transition between the magmatic and hydrothermal stages in volatile-rich magmatic systems (F, B) active in orogenic belts. Their relationships with a nearby batholith are highly debated, with two main genetic processes being frequently opposed as follows: (i) the fractional crystallisation of a parent S-type granitic magma with a progressive enrichment in incompatible elements during differentiation [1–3] or (ii) anatectic-type melting [4]. Such spatial but not necessarily genetic associations are also found in the Segura region in the southern part of the Central Iberian Zone (CIZ) in Portugal, which is close to the Portugal–Spain border. This swarm of aplites and pegmatites was described by [5] in a pioneering study of the main features of these intrusive bodies. Detailed maps of the Segura region enabled a thorough sampling of the granite facies and nearby aplite/pegmatites. They motivated a more detailed study of the mineral succession from the magmatic to hydrothermal stage. There, the pegmatite and aplite dykes are hosted by the surrounding metapelitic schist series but are close to the westernmost edge of the Cabeza de Araya batholith [6–9]. The perphosphorus feature of the dyke magmas is particularly significant, indicating the role of P, F, and Li as fluxing agents. The abundance of these elements results in a specific

mineralogy, especially that of phosphates, which are then particularly sensitive to the evolution of fluids during magma cooling and to the late introduction of external chemical components by hydrothermal fluids.

In the present work, we describe the wide variety of Li, Na, Fe-Mn, and Ca-Sr phosphates found in the aplite dykes and associated pegmatites of the Segura region, with the following objectives: (1) to study the petrographic, mineralogical, textural, and chemical characteristics of the phosphates and establish a paragenetic sequence of the phosphate phases in relation to the magmatic–hydrothermal evolution; (2) to define the geochemical characteristics of the magmas in terms of P, Li, and F evolution; (3) to discuss the origin and behaviour of phosphorus in these magmatic–hydrothermal stages and to understand why several distinct phosphates crystallised in addition to apatite in all the facies at the magmatic stage; and (4) to compare the characteristics of the Segura granites with other similar intrusive suites. The mineralogical and geochemical characteristics of these aplites and pegmatites display similarities to other peraluminous and leucocratic intrusive bodies in the region, such as the Argemela intrusion which is located 30 km to the east [10], as well as with the reference intrusions which are described in detail, such as Beauvoir in the French Massif Central [11] and Tres Arroyos in Spain [3,12,13]. Therefore, a comparison was mainly focused on the range of phosphorus content and its potential role with fluorine on melt mobility.

2. Local Geology

The Segura region is in the southern domain of the CIZ in the easterly part of the Góis–Panasqueira–Argemela–Segura strip, which covers an area rich in granitic intrusions and hydrothermal manifestations associated with different Sn-W-Nb-Ta-Li mineralisation types (Figure 1a). Many studies have reported evidence of Variscan polyphase deformation, metamorphism, and multi-stage magmatism throughout the CIZ [14-17]). However, the bulk of the magmatic intrusions were formed between 320 and 305 Ma, which was roughly concurrent with the Late Variscan deformation and retrograde metamorphism (D3-M3) following the main compressional Late Devonian event and Barrovian metamorphism (D1-M1) as well as the Mississippian regional extensional tectonic event synchronous with Buchan-type metamorphism (D2-M2), which are particularly well described in the northern part of the CIZ. The Late Variscan pluton intrusion was contemporaneous with the D3-M3 upright folding and steep axial plane foliation, thereby defining the present-day regional NW-SE Variscan trend marked by the Ordovician–Silurian synclines and by the conjugated WNW-ESE and ENE-WSW late-D3 regional transcurrent shear zone activity and related structures [15–19].

The CIZ is characterised by the high volume of peraluminous granitic rocks [20] that are syn-to-post kinematic [21–23], and it includes strongly peraluminous, Ca-poor, and variably P-enriched two-mica leucogranites, which are interpreted as being derived from the melting of a metasedimentary source along with several series of metaluminous to weakly peraluminous granites [23,24]. In the Góis–Panasqueira–Argemela–Segura strip, many granite intrusions are peraluminous, like those of Segura, Penamacor, Panasqueira, Orca, and Castelo Branco (Figure 1a). Most of these granites are dated 299–312 Ma with two stages of Li pegmatites at 310 ± 5 and 301 ± 3 Ma ([21]; synthesis in [25]). Some are backed by older intrusions, recording an important magmatic event at the Cambrian-Early Ordovician transition, such as the Fundão, Oledo-Idanha-a-Nova, and Zebreira granites and granodiorites [26,27].

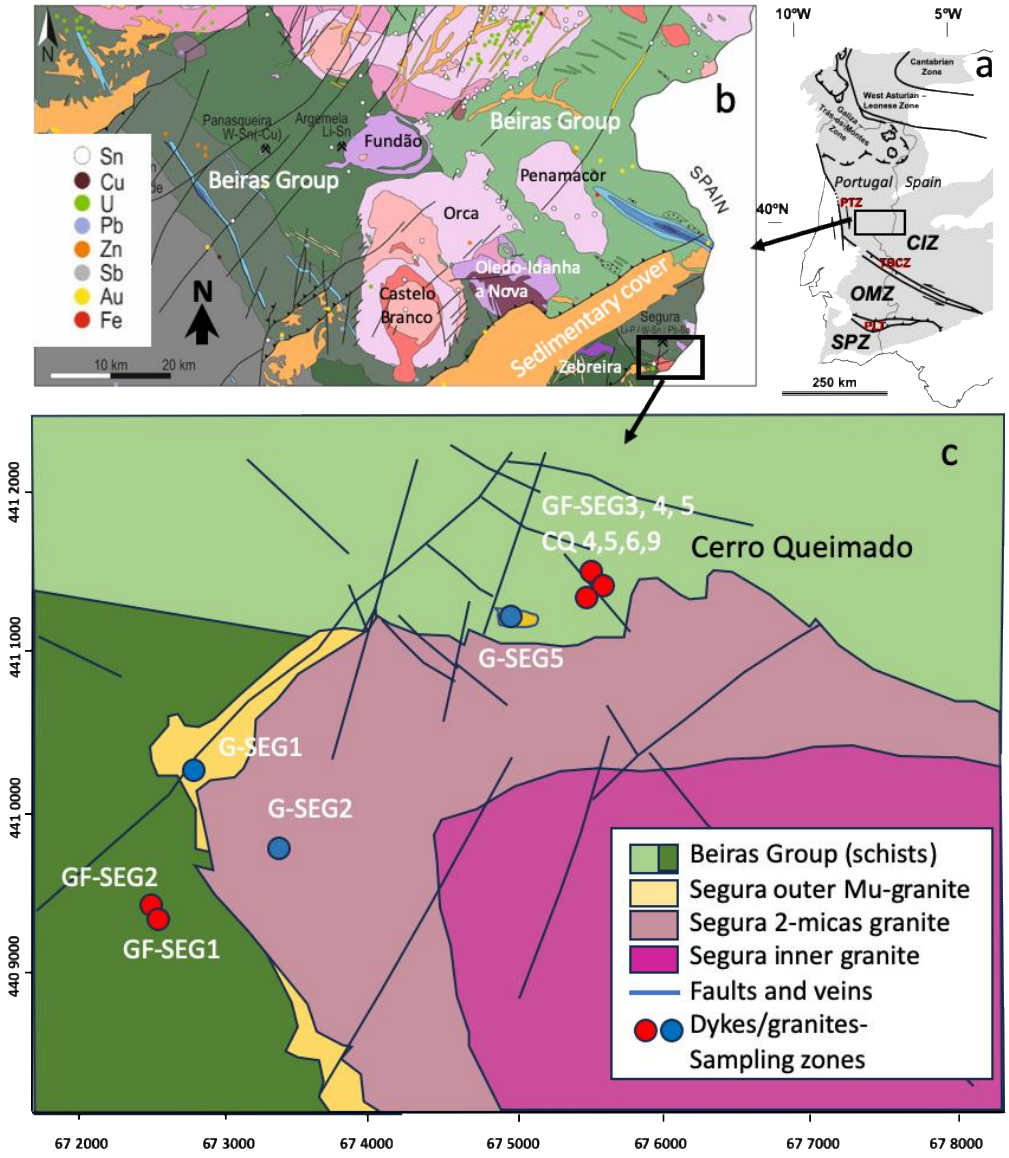

Figure 1. (**a**) Map of main geological units in Portugal and Spain; CIZ—Central Iberian Zone; OMZ—Ossa–Morena Zone; SPZ—South Portuguese Zone; PLT—Pulo do Lobo Terrane (contiguous to the SW Iberian suture); PTZ—Porto–Tomar Shear Zone; TBCSZ—Tomar–Badajoz–Córdoba Shear Zone. (**b**) Simplified map of the Góis–Panasqueira–Argemela–Segura Sn-W strip, which is south of the Central Iberian Zone (CIZ, Portugal) according to the 1:500.000 geological map and the SIORMINP mineral occurrence map of the Portuguese Geological Survey (LNEG) [28]. Different shades of green represent the Beiras Group formations, and the blues the Ordovician–Silurian units defining the upright D3 synclines in this sector of the CIZ NE-SW faults represent late-D3 shear zones that were systematically reactivated in the Alpine orogenic cycle, thus controlling the shapes and disposition of the Cenozoic basins (in orange). The remaining colours represent Cadomian (fuchsia), Ordovician (cherry and dark pink), and Late Variscan (320–300 Ma) granitoids (dark and light orange and light pink). Coloured small circles indicate mineralisation occurrences as in the official SIORMINP catalogue (LNEG). (**c**) Geological setting of the studied Segura area in the north-western border of the Segura–Cabeza de Araya Batholith and an indication of the sample location for dykes. The geological map was adapted from the geological maps of Portugal at 1:500,000 [29]; the coordinate system is WGS 84 29T, UTM (zone 29).

The Segura granites form the westernmost tip of the Cabeza de Araya batholith, near the border between Portugal and Spain (Figure 1). The Cabeza de Araya batholith extends more than 60 km on the Spanish side [7–9], with three sub-facies noted as A, B, and C, thus forming a zoned structure [30]. In the Segura region (Portugal), a zoned edge with

two outer facies, in particular a two-mica facies and a thin border of the so-called outer muscovite-rich granite [5] (Figure 2a–c). The pluton has induced an aureole comprising the contact metamorphism of up to one kilometre. The muscovite-rich and two-mica granite facies exposed in the Segura region have been dated by TIMS U-Pb on zircon [5] at 312.9 Ma and 311 ± 0.5 Ma, respectively.

Figure 2. Outcrops of the aplite–pegmatite dykes and granites in the Segura region. (**a**) Inner facies of the Cabeza de Araya batholith, with large euhedral cordierite crystals (noted Crd) and predominant biotite; (**b**) inner rim of the Cabeza de Araya batholith, showing a two-mica coarse-grained facies with local tourmaline and showing large retrogressed cordierite crystals; (**c**) medium- to-coarse-grained muscovite leucogranite with tourmaline from the outer rim of the Cabeza de Ayara

pluton in Segura region, intruding spotted schists of the Beiras Group (BG); (**d**) low-dipping dyke hosted in BG metasediments in the Cerro Queimado area (see Figure 1b); (**e**) sub-horizontal dyke intrusive in BG metasediments in the Cerro Queimado area; (**f**) aplite dyke from the southern area to the southwest of Segura; (**g**) pegmatite exposure at the level of the river (southwest of the Segura batholith); (**h**,**i**) two other views of the dykes intruding on the metasediments, thereby showing geometric arrays due to the forced intrusion on the schists, which open in several directions and fall as enclaves within the magma.

Considering the hydroxyl apatite crystal's chemistry, as well as the decrease in $^{87}Sr/^{86}Sr$ and the ^{18}O shift to higher values from the two-mica granite to the lepidolite-type aplite–pegmatite dykes, [5] ones concludes that (i) the aplite–pegmatite dykes originate from muscovite granite magma from the fractional crystallisation of quartz, plagioclase, K-feldspar and that (ii) aplites cannot derive from the main two-mica granite and correspond to distinct pulses of magma from the partial melting of heterogeneous metapelitic rocks.

On the Portuguese side, dykes of fine-grained granites (aplites), which are locally associated with pegmatites, intrude on the schist–metagraywacke complex of the Neoproterozoic to Lower Cambrian ages, thereby forming the Beiras Group (BG [31] (Figure 2d–i). There, the greenschist facies metasedimentary rocks are occasionally interbedded with the metaconglomerate layers. Dykes are located in two distinct areas, both on the northern and southwestern flanks of the westernmost end of the Segura pluton. These bodies, trending NE-SW, show low dipping angles (<45°) and are sub-perpendicular to the schists, which are characterised by a vertical or steeply dipping foliation (Figure 2d–f). They are generally around a metre or are exceptionally several metres thick and vary in length from a several decameters to a few hundred metres. Smaller dykes are also observed (Figure 2g–h).

3. Materials and Methods

The methodology used is original and based on mapping phosphorus minerals at the thin section scale by micro-X-ray fluorescence (micro-XRF), followed by imaging and the semi-quantitative investigation of the phosphates by a Scanning Electron Microscope (SEM) equipped with an Energy Dispersive Spectrometer (EDS). Then, a (i) SEM-WDS (Wavelength Dispersive Spectrometer) is used when the complexity of the textures hampers the use of standard electron microprobe analyses (EMPAs) and (ii) an electron microprobe in all other cases. Micro-XRF mapping, SEM, and EPMA measurements were performed at the SCMEM analytical platform of the GeoRessources laboratory, Nancy, France.

This methodology was applied to eighteen thin sections mapped in transmitted light with a Keyence VHX macroscope before micro-XRF mapping on the selected samples to establish the paragenetic sequence of the hydrothermal mineral assemblages. Micro-XRF maps were made choosing the most representative assemblages to render SEM and electron microprobe investigations easier. Micro-XRF mapping was carried out using a M4 Tornado instrument (Bruker Nano Analytics, Berlin, Germany) equipped with an Rh X-ray tube (Be side window) and polycapillary optics, thus giving an X-ray beam with a 25–30 μm diameter on the sample. The X-ray tube was operated at 50 kV and 200 μA. Two 30 mm^2 Xflash® SDD detectors (Bruker Nano Analytics, Berlin, Germany) measured X-rays with an energy resolution of <135 eV at 250,000 cps. All analyses were carried out in a 2 kPa vacuum. The main elements such as Ca, Mg, Mn, Fe, P, Al, K, Na, and Si were mapped, and the composite chemical images were generated. Eleven samples were mapped to depict the mineral assemblages in the veins and their chemical zoning (phosphates).

SEM investigations were performed on eight samples using a JEOL JSM-7600F Schottky-FEG-SEM (JEOL Ltd, Tokyo, Japan) equipped with an Oxford Instruments 20 mm^2 SDD-type EDS spectrometer (Oxford Instruments plc, Abingdon, UK). All elements (including trace elements) have standard deviations (2σ) of less than 10%.

Quantitative analysis of the major elements was performed with a CAMECA SX100 EPMA (CAMECA SAS, Gennevilliers, France) equipped with five WDS spectrometers using an accelerating voltage of 15 kV, a probe current of 12 nA (an accelerating voltage of 25 kV and a probe current of 150 nA for trace elements), and a beam diameter of 1 μm. The peak and background counting times were 10 and 5 s, respectively. The following crystals were used: TAP (F, Na, Mg, Al, Si, and Rb), LPET (K, Cl, and Nb), LiF (Mn and Fe), and PET (Cs). The standards were natural minerals and synthetic oxides as follows: topaz (FKα), albite (Na, SiKα), olivine (MgKα), andradite (CaKα), Al_2O_3 (AlKα), orthoclase (KKα), $MnTiO_3$ (Mn, TiKα), Fe_2O_3 (FeKα), $RbTiPO_5$ (RbLα), $SrSO_4$ (SrLα), and barite (BaLα).

The phosphate crystals were examined with an HR Horiba Jobin Yvon Raman system (Jobin Yvon, Longjumeau, France) (GeoRessources laboratory, Nancy, France) using a 514.5 nm Ar^+ laser emission line at a resolution of 2 cm^{-1} in the 100–4000 cm^{-1} range. Repeated acquisition using the highest magnification was accumulated to improve the signal-to-noise ratio. Raman spectra were generally obtained after five acquisitions of 10 to 20 s each, both in the low-frequency (200–1200 cm^{-1}) and high-frequency ranges (3550–3800 cm^{-1}).

Whole-rock major and trace element analyses were performed on field samples at the «Service d'Analyse des Roches et des Minéraux (SARM)», Centre de Recherches Pétrographiques et Géochimiques (CRPG), Nancy, France. Major elements were analysed by inductively coupled plasma optical emission spectrometry on a Thermo-Fischer ICap 6500 instrument (Thermo-Fischer Scientific, Waltham, USA). Trace elements, including rare earth elements (REEs), were determined by inductively coupled plasma mass spectrometry (Thermo-Elemental X7) (Thermo-Fischer Scientific, Waltham, USA). Detailed analytical procedures are given in [32]. For three samples, data were obtained by an XRF analytical tool at Lisboa University, and the loss on ignition (L.O.I.) was not determined but estimated by difference to 100%.

4. Results

4.1. Field Observations

Two main aplite–pegmatite swarms were distinguished, which was mainly based on field relationships, the mineralogical and geochemical data detailed below, and structural and textural characteristics.

In the northern border of the Segura pluton, there is the so-called "Cerro Queimado" mining area where banded aplite–pegmatite dykes are intrusive and have filled sub-horizontally opened fractures in the metasedimentary sequence. They are sub-perpendicular to the foliation, striking N140° and dipping between 20 and 45° to the south (Figures 1b and 2a,b). Other low-dipping (<30° to the south–southwest), N135°–150° aplite–pegmatite dykes are found in the southern border of the most occidental part of the Segura pluton (Figure 1b). They occur as multi-decimetric-thick to metre-thick intrusions, which are well exposed in the river valley (Figure 2c–f).

In both pegmatite and aplite bodies, albite, K-feldspars, and quartz are the main constituents, with both minerals forming bands parallel to the boundary with the host schist (Figure 3a). Pegmatite develops as infillings of the opened fractures within the aplite dykes, usually displaying growth textures that are perpendicular to the aplite boundary (Figure 3b). A series of phosphates, like amblygonite and other (Fe-Mn, Ca-Sr)-P phases, Nb-Ta oxides, and topaz are abundant. Both aplites and pegmatites are leucocratic magmatic facies with low amounts of black constituents, except Nb-Ta oxides and local tourmaline.

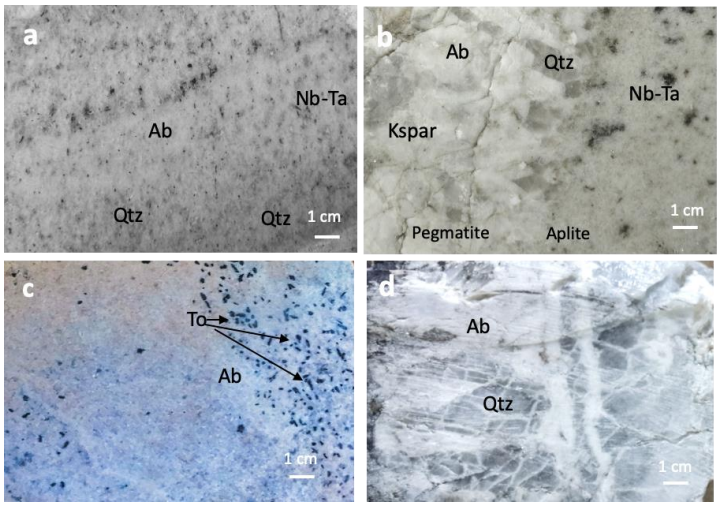

Figure 3. Textures of the Segura dykes. (**a**,**b**) Contact between the aplite and pegmatite in the samples from the northern zone of the Segura batholith (Cerro Queimado). Facies are leucocratic with black dots corresponding to the Nb-Ta oxides (Nb-Ta). The development of pegmatite occurs through the growth of albite (Ab) and quartz (Qtz) as subparallel crystals and minor K-feldspar (Kspar). (**c**) Macroscopic feature of the tourmaline (To) bearing aplite from the southern zone of the Segura dyke swarm. (**d**) Pegmatite with comb quartz and albite development.

Thus, tourmaline is only found in places in the northern swarm and is not abundant. In contrast, tourmaline-rich aplite dykes occur in the southern swarm (Figure 3c).

Some of the dykes are affected by later magmatic–hydrothermal stages, thereby resulting either in the abundant formation of quartz (Figure 3d) or lepidolite that is associated with cassiterite. The latter assemblage is not the subject of the present work.

4.2. Dyke Mineralogy

Detailed composite chemical maps of the mineral assemblages were obtained using micro-XRF and are presented in Figure 4. In Figure 4a,b, the typical texture of the pegmatite developed onto aplite is characterised by the crystallisation of euhedral quartz prisms and tabular albite perpendicular to the aplite boundary. Li-Na phosphates (amblygonite series) form euhedral crystals subparallel to the quartz prisms and tabular albite or are crystallised onto the euhedral K-feldspars and albite. They are also included as small patches within quartz. The mineral assemblage generally ends by filling the remaining space with K-feldspar (Figure 4a) or, most frequently, quartz (Figure 4b–d).

The Fe-Mn phosphates are tiny euhedral crystals found within or on albite, which are frequently at the boundary with the Li-Na-phosphates and seem synchronous with albite. Albite corrodes the quartz that is deposited as the euhedral crystal palisade onto the aplite and is accompanied by topaz. Albite also corrodes the K-feldspars. Synchronous to the albite stage, Na-rich phosphate replaces the Li phosphate from the amblygonite series. Apatite later invades the early texture, thereby forming euhedral needles and microdomains within the albite and earlier phosphate, which frequently occurs along the former grain boundaries (microdomains presented in orange in Figure 4e,f). Identifying the few grains of magmatic apatite is difficult because most of the feldspars are rich in small apatite inclusions or needles linked to hydrothermal alteration.

The Na-Li phosphates show complex textures and relationships. Crystals of the amblygonite series are the first phosphate to crystallise as large and sometimes centimetric crystals (sample GF-SEG3). They are frequently euhedral, and sometimes centimetric prisms are oriented perpendicular to the aplite layers and grow towards the centre of the pegmatite veins (microdomain in the yellow-green colour in Figure 5a–c). They are associated with topaz, which appears in red in the composite micro-XRF maps from Figure 5c,d. These large crystals are partially replaced by the Na-Al phosphates (lacroixite),

which form replacement patches at the microscale. Microdomains are a few dozen micrometres long within the initial mass of the Li-phosphate (Figure 5e,f). This pervasive replacement thus yields a mixture of the two phases (montebrasite, lacroixite) at the microscale (Figure 5f).

In addition to the Li (Al, Na) phosphates, Fe-Mn (Al) phosphates crystallised, apparently relatively early as isolated grains (Figure 5c, inset noted g, h and enlargements in Figure 5g,h). Fe-Mn phosphates show alternated Fe-rich and Mn-rich growth zones with euhedral development, indicating their early formation in the melt before being included in albite crystals. They are coated by a late overgrowth enriched in iron, which finally develops in micro-fissures nearby where insufficient growth space is available, probably during a relatively late stage (Figure 5h). The external rim corresponds to a late overgrowth, which fills minor fractures of the surrounding albite around the initial crystal and is particularly enriched in iron. Raman spectra have shown that the phosphate belongs to the eosphorite–childrenite solid solution (see below Raman and crystal-chemistry data).

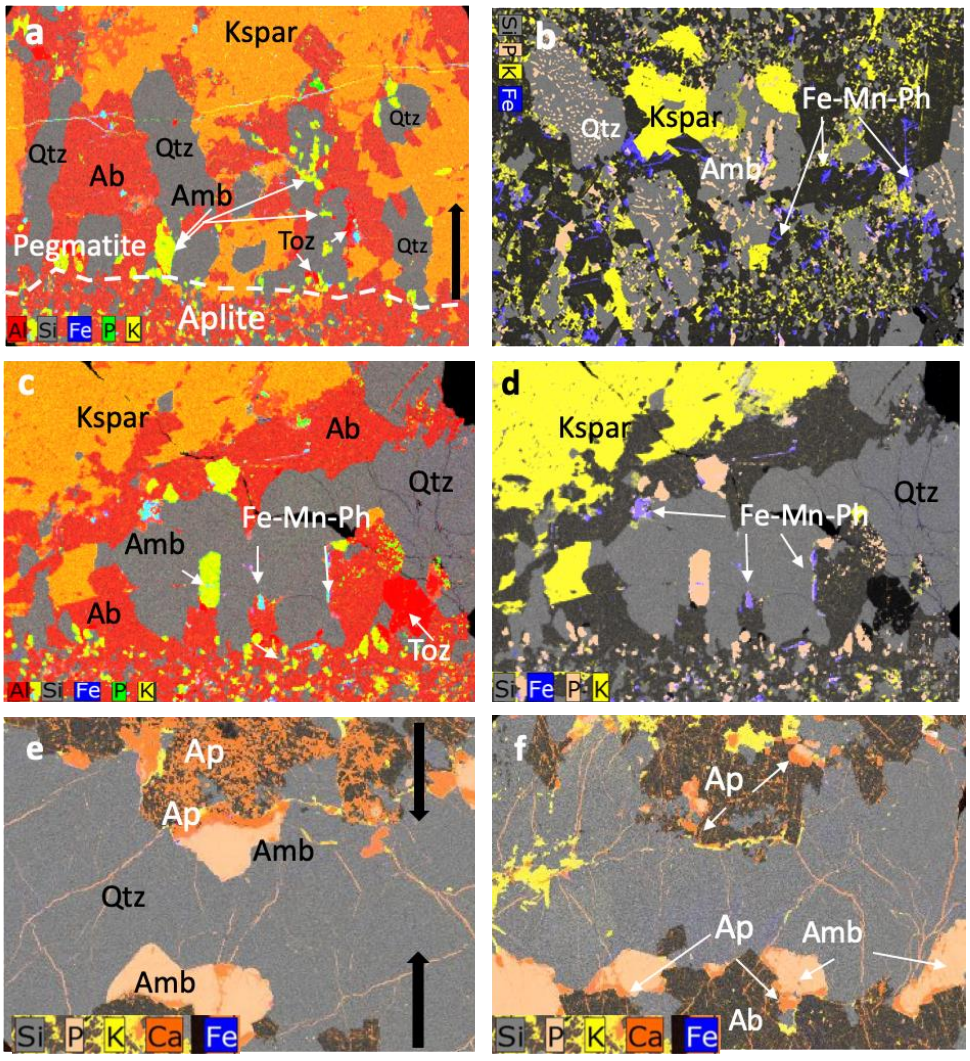

Figure 4. Composite micro-XRF chemical maps of aplite and pegmatite dykes. (**a**) Boundary between aplite and pegmatite showing the growth of albite (in red), quartz (grey), and amblygonite (light yellow) perpendicularly to the boundary, as well as K-feldspar (in orange: Al, K); (**b**) pegmatite texture with phosphates included in quartz; (**c**) amblygonite (in green-yellow), albite, K-feldspar, and quartz; (**d**) same chemical map with the Fe phosphate in violet-blue; (**e**) amblygonite on both sides of the cavities filled with quartz (black arrow indicates how the cavity has been filled) and apatite (in orange) replaces the K-feldspars; (**f**) amblygonite as euhedral crystals formed on albite and cemented by quartz and, in orange, apatite filling microfractures. Toz: topaz; Amb:

amblygonite; Fe-Mn Ph: eosphorite–childrenite Fe-Mn phosphate series; Kspar: K-feldspar; Ab: albite; Ap: apatite; Qtz: quartz.

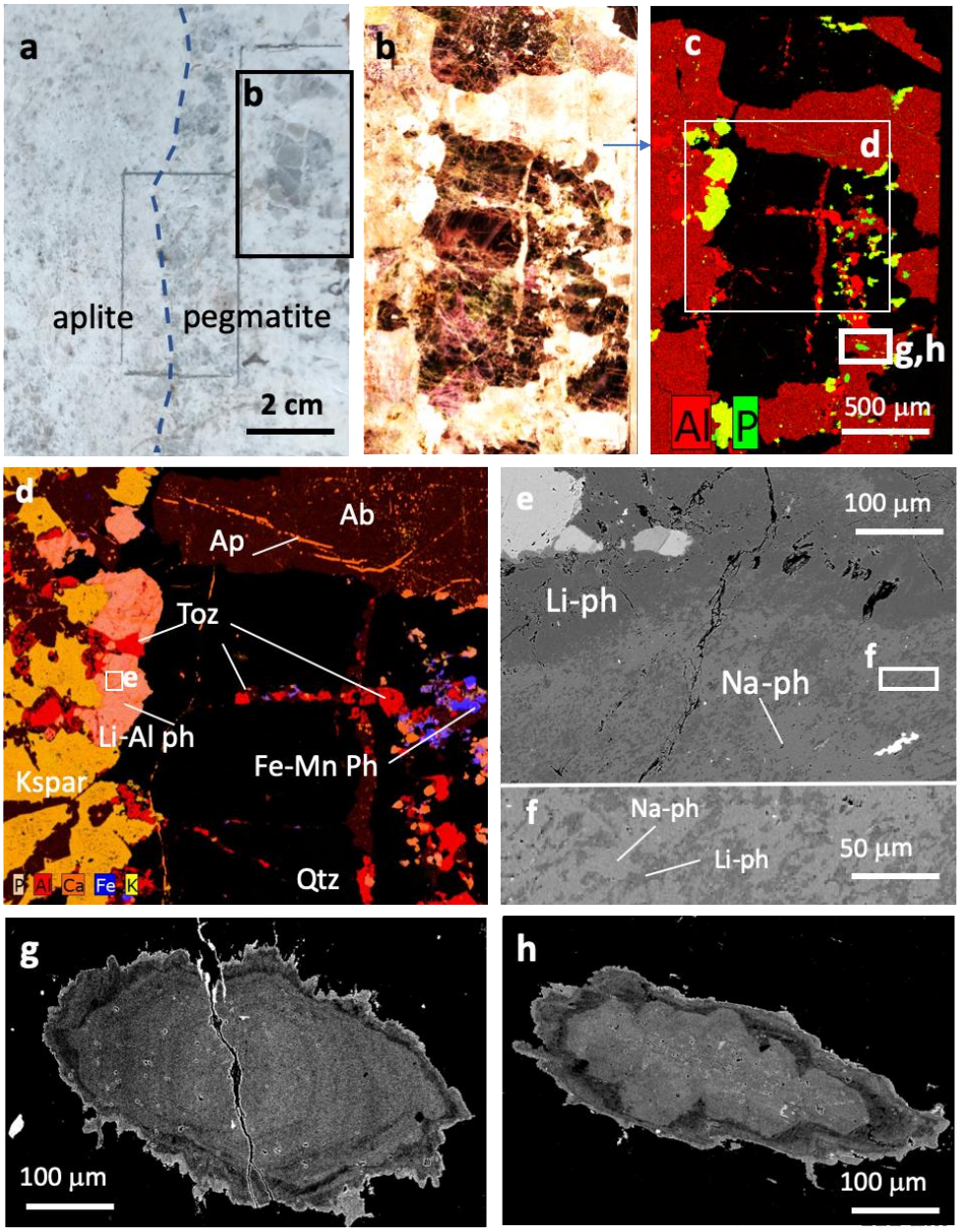

Figure 5. (**a**) Boundary between aplite and pegmatite (macroscopic photograph), with an indication of the zone mapped in figures (**b**,**c**); (**b**) transmitted light microphotograph of the thick section; (**c**) chemical micro-XRF map showing amblygonite (yellow) on both sides of the cavity filled with quartz and the Fe-Mn phosphate (in green); (**d**) magnified detail of zone (**c**) showing the distribution of the amblygonite formed onto K-feldspars and topaz as inclusions in quartz (in red); (**e**) microtextures of Li-phosphates (Li-ph) (amblygonite and mixed lacroixite/amblygonite); (**f**) magnification of the amblygonite/lacroixite at the micron scale; (**g**,**h**) crystals of Fe-Mn phosphates (BSE SEM image), showing the euhedral growth bands. Toz: topaz; Li-ph: Li phosphates; Amb: amblygonite; Na-ph: Na-phosphate (lacroixite-dominated); Fe-Mn-Ph: eosphorite–childrenite Fe-Mn phosphate series; Kspar: K-feldspar; Ab: albite; Ap: apatite; Qtz: quartz.

Crandallite forms at the grain boundary or, at the expense of earlier phosphates, replaces them, particularly Li-Na-phosphates, as shown in Figure 6a. Figure 6b,c illustrate the microscopic aspect of the amblygonite crystal, showing an intense alteration at the boundary with albite. Microdomains are small, ranging from a few microns to tens of

micrometres, and they are very complex at a small scale, as shown by the enlargement from Figure 6d. Along the microfissures affecting the amblygonite (Figure 6d), goyazite–crandallite develops as euhedral crystals with a very large composition between domains characterized by variation in the mean atomic number "Z" (from dark grey to light grey), corresponding to the Ca-Sr exchange (Figure 6e).

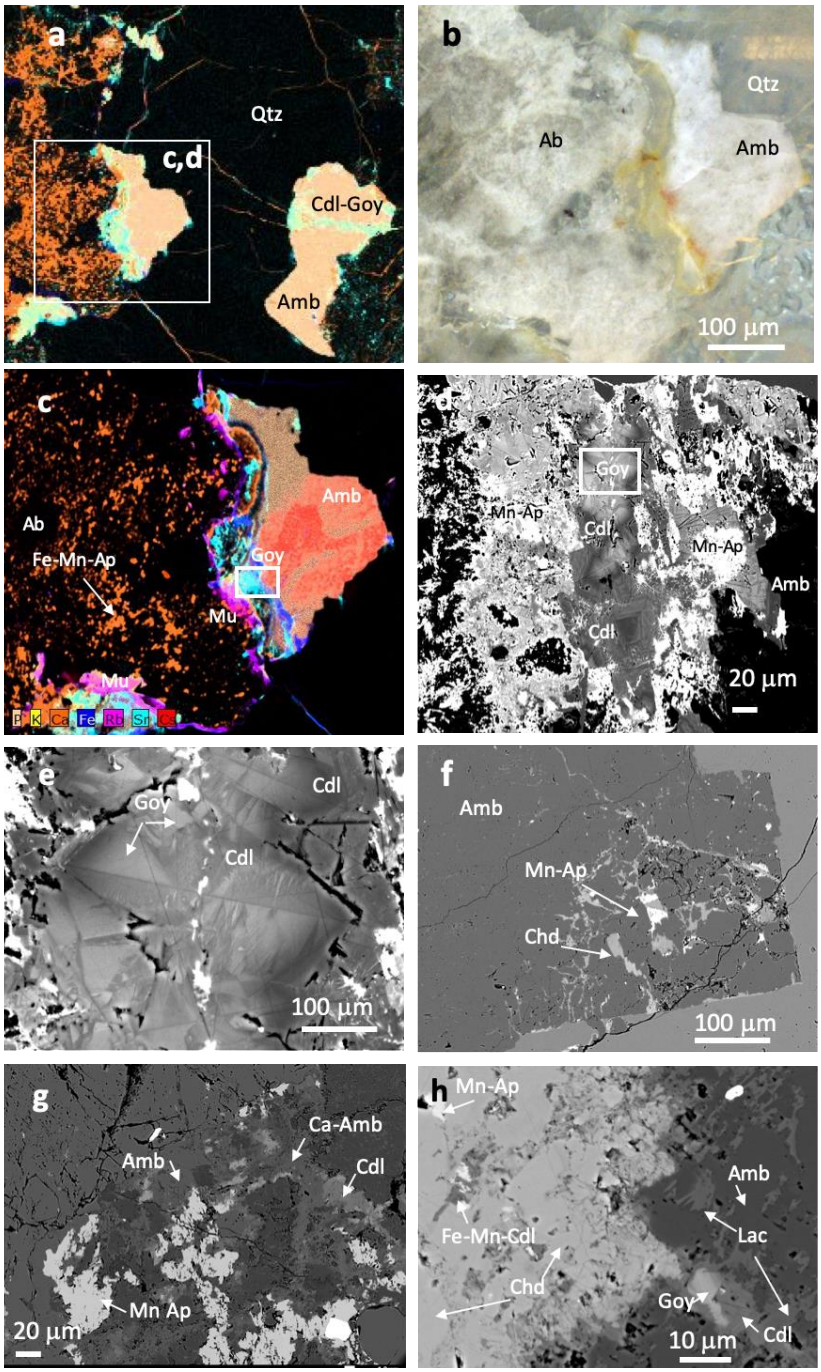

Figure 6. (**a**) Amblygonite crystals developed on the edge of a cavity filled with quartz; (**b**) crandallite and Fe-Mn-rich apatite formed in microfractures; (**c**) detail of the amblygonite crystal of figure (**a**); (**d**) micro-XRF composite chemical map showing the replacement of amblygonite by complex assemblages of phosphates at the boundary between the crystal and feldspars; (**e**) detail of the complex zone of replacement formed by crandallite and goyazite and later Mn-rich apatite; (**f**) detail of the growth bands of the goyazite crystals with the earliest bands of crandallite; (**g**) complex association of phosphates replacing amblygonite. Amblygonite may contain calcium with no clear evidence of the addition of crandallite patches, and apatite is enriched in Fe and Mn; (**h**) association of

the four types of phosphates with mutual replacements, with the same abbreviations as those in Figure 4; Goy: goyazite; Cdl: crandallite; Chd: chidrenite; Lac: lacroixite; Mn-Ap: Mn-rich apatite; Qtz: quartz; and Mu: muscovite.

Apatite grains grow as patches in feldspars, especially albite (Figure 6c). They also locally replace all the earlier phosphate types and fill pores and microfractures, thereby developing needles, plumose crystals, or microdomains as grain aggregates (Figure 6f,g). In the tourmaline-rich aplites of the southern swarm, apatite forms poikilitic aggregates around quartz, mica, and tourmaline. The apatite composition is heterogeneous, incorporating significant amounts of Al, Fe, Mn, and traces of Sr. When these element concentrations increase, the fluorine concentration decreases, suggesting an increase in OH at the expense of fluorine when shifting from the ideal F apatite stoichiometry.

4.2.1. Raman Data on Phosphates

All phosphates were analysed by Raman spectroscopy. The three main solid solutions (eosphorite–childrenite, amblygonite-lacroixite, and crandallite–goyazite) are confirmed by comparison with the reference spectra from the international database RRUFF [33]. The most representative spectra are presented in Figure 7. For the eosphorite-chidrenite series ((Fe, Mn) $AlPO_4(OH)_2(H_2O)$), Raman spectroscopy enabled the observation of bands at 969 cm^{-1} and 1018 cm^{-1}, which were assigned to the phosphate bonds. For the other peaks, the assigning proposed by [34] is as follows following: Raman bands at 562 cm^{-1}, 595 cm^{-1}, and 608 cm^{-1} are assigned to the ν4 bending modes of the PO_4, HPO_4, and H_2PO_4 units; Raman bands at 405, 427, and 466 cm^{-1} are attributed to the ν2 modes of these units. Hydroxyl and water stretching bands are also observed at 3200–3500 cm^{-1}. Differences between the peaks of eosphorite and childrenite are a function of the abundance of manganese and mostly concern the peak at 253, 557, 618, and 1053 cm^{-1} noted in italics in Figure 7a.

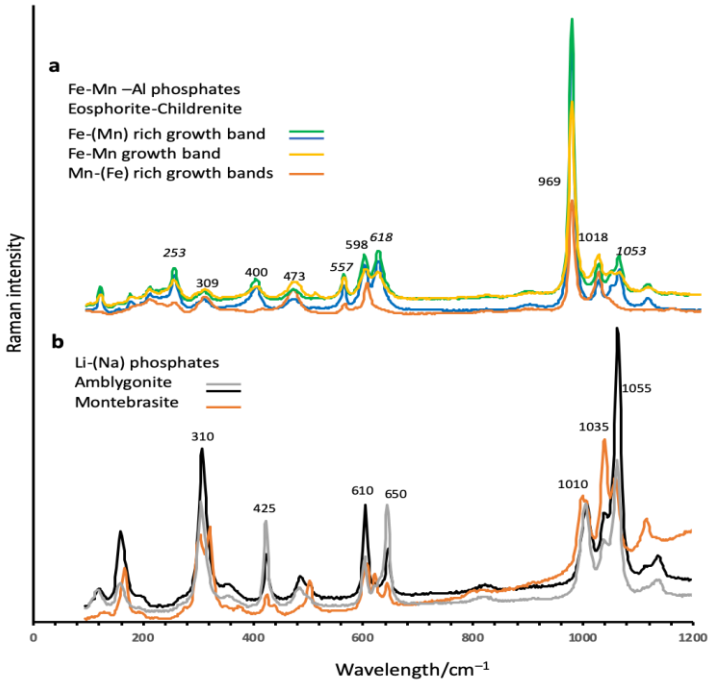

Figure 7. Representative Raman spectra of two phosphate series. (**a**) The eosphorite–childrenite series and (**b**) the Li phosphate series represented by amblygonite and intermediate phases with a spectrum closer to montebrasite.

The Raman spectra for the amblygonite–montebrasite series are presented in Figure 7b. Most spectra display intermediate features between amblygonite and montebrasite, which are typical of the natural series of such minerals. The main changes as a function of the fluorine content concern a few peaks [35], particularly from 599 to 604 cm^{-1} and between 1056 and 1066 cm^{-1}. The spectra present a series of peaks between 1050 and 1056 cm^{-1}, which are closer to the montebrasite following [35]. Significant differences occur between 3379 and 3348 cm^{-1} (not shown in Figure 7).

4.2.2. Crystal Chemistry of Phosphates

The crystal chemistry of the analysed phosphates is shown in Figure 8. The different series are the following: eosphorite–childrenite, the montebrasite–amblygonite–lacroixite series, crandallite–goyazite, and apatite.

Eosphorite–childrenite displays a significant Fe-Mn substitution (Table 1), which is found in all the crystals, as illustrated by Figure 8a, for three distinct crystals. In the external rim, more than 22% FeO is reached for 4 to 5.3% MnO. They contain low amounts of magnesium (MgO ranges from 0.1 to 1.3%). Still, the main zoning corresponds to a significant Fe and Mn concentration fluctuation with a Fe/Fe + Mn ratio varying from 0.3 to 0.7.

Table 1. Representative analyses and corresponding structural formulae of the Fe-Mn-rich phosphate series (eosphorite–childrenite) from the Segura dykes.

weight%	**Phosphates from the Eosphorite-Childrenite series**							
MgO	0.97	0.18	0.29	n.d.	0.08	0.16	0.18	0.21
Al_2O_3	22.68	22.89	22.99	21.98	22.16	22.18	21.96	22.47
P_2O_5	31.23	30.89	30.27	29.54	30.3	29.81	30.4	30.36
CaO	0.27	0.15	0.26	n.d.	0.02	0.14	0.06	n.d.
FeO	9.51	11.91	13.37	15.64	18.01	18.65	21.90	22.49
MnO	21.35	18.28	17.72	14.24	11.86	11.65	8.72	8.7
total	87.07	85.63	86.39	83.14	84.44	84.67	85.66	86.74
a.p.f.u.	**Structural formulae**							
Mg	0.05	0.01	0.02	0.00	0.00	0.01	0.01	0.01
Al	1.01	1.03	1.06	1.04	1.02	1.04	1.01	1.03
P	1	1	1	1	1	1	1	1
Ca	0.01	0.01	0.01	0	0	0.01	0	0
Fe	0.30	0.38	0.44	0.52	0.59	0.62	0.71	0.73
Mn	0.68	0.59	0.59	0.48	0.39	0.39	0.29	0.29
Fe + Mn	0.98	0.97	1.01	1.03	0.98	1.01	1.00	1.02
Fe/(Fe + Mn)	0.31	0.39	0.43	0.52	0.60	0.61	0.71	0.72

The montebrasite–amblygonite series represents the predominant Li-Al phosphate end-members (Figure 8b, Table 2). They are characterised by variable (OH, F) contents and a systematic replacement by lacroixite (Na-Al end-member). Lacroixite is probably physically mixed with the former montebrasite–amblygonite as compositions do not enrich the Na-end-member. The data points with a ratio of Na/Na+ Li that is higher than 0.5 are scarce (Table 2). Mixed analyses cannot be precluded as the lacroixite microdomains are relatively small (Figure 8b). n.d.: not determined.

Table 2. Representative analyses and corresponding structural formulae of the Li-Na-rich phosphate series (amblygonite-lacroixite) from the Segura dykes.

Weight %		**Lacroixite**		**Amblygonite**	
Na_2O	14.37	15.63	15.92	0.03	0.04
MgO	0.00	0.00	0.00	0.00	0.04
Al_2O_3	31.62	31.31	32.40	35.33	34.32
P_2O_5	45.13	43.24	43.54	47.55	48.04
CaO	0.00	0.00	0.00	0.06	0.09
FeO	0.00	0.00	0.00	0.08	0.06
MnO	0.00	0.00	0.00	0.04	0.00
F	12.50	12.54	11.74	6.07	6.32
H_2O*	0.00	0.00	0.56	3.78	3.00
Li_2O*	2.57	1.57	1.49	9.99	10.09
Total	105.57	103.97	105.65	102.94	102.01
O=F	5.26	5.28	4.94	2.56	2.66
Total*	100.31	98.69	100.71	100.38	99.35
a.p.f.u.			**Structural formulae**		
Na	0.73	0.83	0.84	0.00	0.00
Li	0.27	0.17	0.16	1.00	1.00
Mg	0.00	0.00	0.00	0.00	0.00
Al	0.98	1.01	1.04	1.03	0.99
P	1.00	1.00	1.00	1.00	1.00
Ca	0.00	0.00	0.00	0.00	0.00
Fe	0.00	0.00	0.00	0.00	0.00
Mn	0.00	0.00	0.00	0.00	0.00
OH	0.00	0.00	0.10	0.63	0.49
F	1.03	1.08	1.01	0.48	0.49

Crandallite–goyazite (Ca-Sr end-member) show a high variation in the Ca or Sr contents and additional cations such as Ba (Figure 8c, Table 3). The divalent cation site is partly vacant, as shown in Figure 8c. The solid solution is mainly in the crandallite field as the ratio of Ca/Ca + Sr is mostly above 0.5. F-apatite, and (F-OH) Al-Fe-Mn-rich apatite end-members are also found with stoichiometry close to apatite but with variable Mn contents.*: asterisk corresponds to calculated values taking into account charge balance.

Table 3. Representative analyses and corresponding structural formulae of the Ca-Sr-rich phosphate series (goyazite–crandallite) from the Segura dykes. *: asterisk corresponds to calculated values taking into account charge balance.

Weight %	**Phosphates from the Goyazite-Crandallite series**								
Na_2O	0.00	0.00	0.24	0.00	0.15	0.12	0.21	0.00	0.00
MgO	0.35	0.00	0.26	0.00	0.17	0.17	0.18	0.00	0.00
Al_2O_3	33.99	33.34	34.51	33.40	34.15	33.40	35.50	35.15	35.98
P_2O_5	32.43	31.82	32.12	31.42	31.60	30.61	32.76	34.22	33.26
CaO	4.26	4.62	6.44	7.49	8.83	9.51	9.40	10.75	11.18
FeO	0.00	0.00	0.14	0.00	0.04	0.00	0.37	0.00	0.00
MnO	0.00	0.00	0.00	0.00	0.15	0.01	0.00	0.00	0.00
SrO	14.58	14.08	10.60	8.17	7.69	6.01	5.51	3.61	0.59
BaO	0.00	0.00	0.00	0.00	0.40	0.00	0.05	0.00	0.00
F	3.90	3.35	2.68	4.11	2.22	2.10	1.19	1.97	3.49
O=F	1.64	1.41	1.12	1.72	0.93	0.88	0.50	0.83	1.46
Total	85.61	83.86	87.10	80.48	86.13	83.32	85.29	83.73	81.01
H_2O*	12.75	14.73	14.57	17.80	16.29	19.29	15.57	15.44	17.53
Total*	87.25	85.27	85.43	82.20	83.71	80.71	84.43	84.56	82.47
a.p.f.u.	**Structural formulae**								
Na	0.00	0.00	0.03	0.00	0.02	0.02	0.03	0.00	0.00
Mg	0.04	0.00	0.03	0.00	0.02	0.02	0.02	0.00	0.00
Al	2.92	2.92	2.99	2.96	3.01	3.04	3.02	2.86	3.01
P	2.00	2.00	2.00	2.00	2.00	2.00	2.00	2.00	2.00
Ca	0.33	0.37	0.51	0.60	0.71	0.79	0.73	0.80	0.85
Fe	0.00	0.00	0.00	0.00	0.00	0.00	0.00	0.00	0.00
Mn	0.00	0.00	0.00	0.00	0.01	0.00	0.00	0.00	0.00
Sr	0.41	0.40	0.31	0.23	0.22	0.18	0.16	0.10	0.02
Ba	0.00	0.00	0.00	0.00	0.01	0.00	0.00	0.00	0.00
R^{2+}	0.78	0.76	0.84	0.84	0.97	0.98	0.91	0.89	0.87
Ca/(Ca+ Sr)	0.89	0.96	1.25	1.44	1.52	1.63	1.64	1.78	1.96
F	0.00	0.79	0.62	0.98	0.53	0.51	0.27	0.43	0.78
OH	4.32	3.50	4.07	3.58	4.47	4.59	4.63	3.94	3.99
F+OH	4.32	4.28	4.69	4.56	4.99	5.10	4.90	4.37	4.77

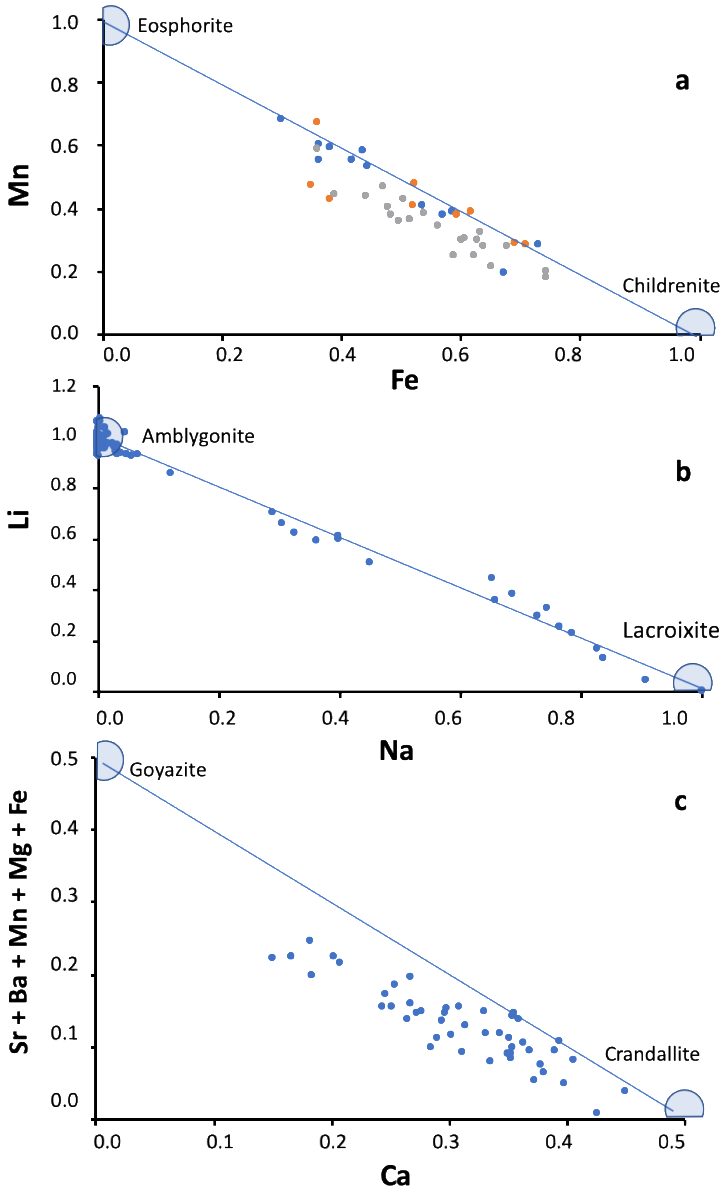

Figure 8. (**a**) Fe and Mn (apfu) in Fe-Mn phosphates (base P = 1) for three distinct crystals represented by three distinct colors. The figure shows that the amplitude of the Fe-Mn exchange covers the same range in each crystal. (**b**) Na versus Li (apfu) diagram for the Na-Li (lacroixite) phosphates (montebrasite–amblygonite) series. The intermediate composition corresponds to the partial replacement of the Na-Li-end-members by the Na-end-member. (**c**) Ca versus the Sr (apfu) plot for the crandallite–goyazite series.

4.3. Geochemistry of Aplite and Pegmatite Dykes from Segura

All the dykes correspond to fractionated aplite–pegmatites enriched in P, Li, F, and to a lesser extent B (for one type of tourmaline-rich aplite). These rocks represent highly differentiated magmas, similar to the LCT facies under the rare element Li subclass of the complex type of classification that is used in [36]. New chemical analyses of granites, aplites, and pegmatites from Segura were obtained on a series of collected samples, as indicated in Figure 1 and reported in Table 4. They were compared with data from previous works (four mean analyses only available from [5]) on the same region and with similar intrusive granite bodies (Argemela: [10], Panasqueira: [37]), Tres Arroyos [3], and Beauvoir (B1 facies, [11]).

The SiO_2 contents displayed by the Segura facies range from 72.2 to 74.0 wt% in the granites and from 73.3 to 74.8 wt% SiO_2 in the aplite–pegmatite bodies, being comparable to the values recorded for the Panasqueira granites (72.5–75 wt% SiO_2) but slightly more siliceous than the Argemela granites (66–72 wt% SiO_2). The Segura granites display intermediate features between the rather albitic facies from Argemela and the most evolved, albite-rich Panasqueira granites. The K_2O to Na_2O ratios range between 0.7 and 1.2 and are thus lower than the Panasqueira granites (0.5 and 3.1) and higher than the Argemela granites (0.2 to 0.7). The enrichment in Na_2O depicts the differentiation and the more albitic feature of the evolved magmas (Figure 9).

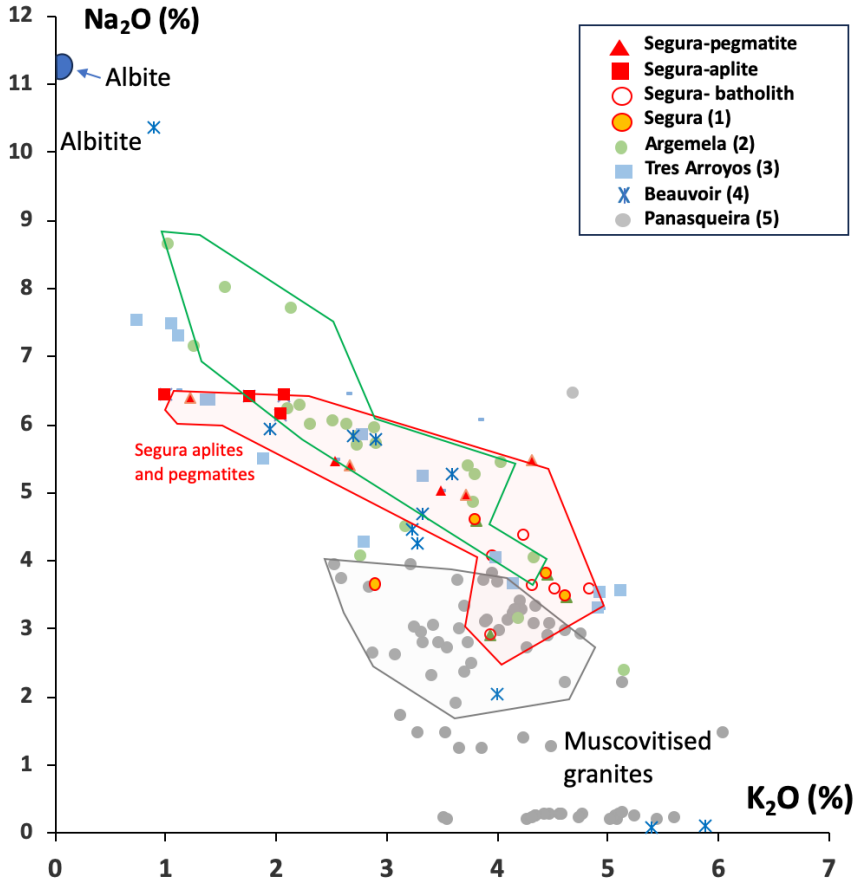

Figure 9. Na_2O versus K_2O diagram for the Segura aplites, pegmatites, and granites. Data are compared with those from the literature as follows: 1: Segura [5], 2: Argemela [10], 3: Tres Arroyos [3], 4: Beauvoir [11], and 5: Panasqueira [37]. Enveloppe colors correspond to data point colors.

Table 4. Representative analyses of pegmatites and aplites from the Segura dyke pairs of aplites and pegmatites noted, with CQ-4, -5, -6, and -9 being adjacent samples and each pair being from the same dyke. bld: below the detection limit. In the three samples, loss on ignition (L.O.I.) was not determined but estimated by difference (*).

	Pegmatite						Aplite						
wt.%	**GF SEG1**	**GF SEG4**	**Peg CQ-5**	**Peg CQ-6**	**Peg CQ-9**	**Peg CQ-4**	**GF SEG-3**	**GF SEG-2**	**GF SEG-5**	**Apl CQ-4**	**Apl CQ-5**	**Apl CQ-6**	**Apl CQ-9**
SiO_2	76.78	69.19	64.04	71.54	70.57	69.29	70.19	70.99	71.74	69.83	69.53	71.19	69.69
TiO_2	0.01	bdl	bdl	bdl	bdl	bdl	0.005	0.02	0.005	bdl	bdl	bdl	bdl
Al_2O_3	13.43	14.77	18.71	15.12	15.36	16.41	16.85	15.33	16.63	16.47	17.84	16.42	16.12
Fe_2O_3	0.19	0.19	0.413	0.159	0.069	0.073	0.76	1.13	0.76	0.171	0.389	0.268	0.167
MnO	0.006	0.024	0.095	0.021	0.000	0.000	0.078	0.048	0.052	0.020	0.089	0.023	0.017
MgO	bdl	bdl	bdl	bdl	bdl	bdl	0.020	bdl	0.010	bdl	bdl	bdl	bdl

CaO	0.3	0.22	0.31	0.74	0.53	0.53	0.18	0.51	0.22	0.70	0.22	0.53	0.85
Na_2O	6.49	6.06	6.39	5.40	4.96	5.48	6.45	5.03	5.48	6.43	6.45	6.42	6.15
K_2O	1.12	3.85	1.22	2.68	3.72	4.31	2.66	3.5	2.54	2.08	1.00	1.77	2.05
P_2O_5	0.46	1.7	4.76	2.49	3.72	2.63	2.43	1.00	1.94	2.29	2.05	2.05	2.38
L.O.I.	1.21*	4.00*	2.11	1.32	1.28	1.19	1.11	n.d.	1.2	1.51	1.61	1.6	1.75
Total	98.79	96.00	98.05	99.47	100.21	99.92	101.43	97.56	100.98	99.50	99.18	100.26	99.17
Li -ppm	n.d.	1160	3278	704	1718	818	n.d.	1000	n.d.	157	1543	304	141
F -ppm	1123	2900	19100	3300	3900	2800	2805	2100	1806	3100	18200	3400	3200

They are similar to the Beauvoir B1 and Tres Arroyos facies and are largely superimposed on most Argemela facies. All these granites are significantly enriched in sodium compared with the Panasqueira granite.

Mafic components are low to very low, with the FeO + MgO + TiO_2 sum being comprised between 0.14 and 1.40, being much lower than in the Panasqueira granites (1.71 and 3.12 wt%) and either similar or higher than in the Argemela ones (0.03 to 0.19). All the rocks are magnesium-poor, with the M index (M = 100Mg/Mg + ∑Fe) being between 8 and 45, similarly to the Panasqueira (15 to 31) and Argemela granites (6 to 46). The magmatic trends are more evident to decipher at Segura and Argemela in the geochemical diagram Al-(K + Na + 2Ca) versus the Fe + Mg + Ti diagram from [38], where the parameter A increases as B decreases. All the rocks are distinctly peraluminous (Figure 10).

At Panasqueira, the peraluminous parameter Al-(K + Na + 2Ca) is, however, increased by the superimposed alteration effects, which is evident for the most altered facies but also perceptible for many of the less modified granite facies [37]. The Segura aplite and pegmatite dykes are significantly enriched in phosphorous, with the P_2O_5 contents in the 0.36 to 2.23 wt% range being higher than the Panasqueira granites (0.23 to 0.74 wt%). Compared with the Panasqueira granites, which are dominated by a strong correlation between the phosphorous and calcium content meaning that the two elements are both entirely contained in apatite (Figure 11), the Segura aplite–pegmatite veins are characterised by an excess in phosphorus, which is not linked to apatite.

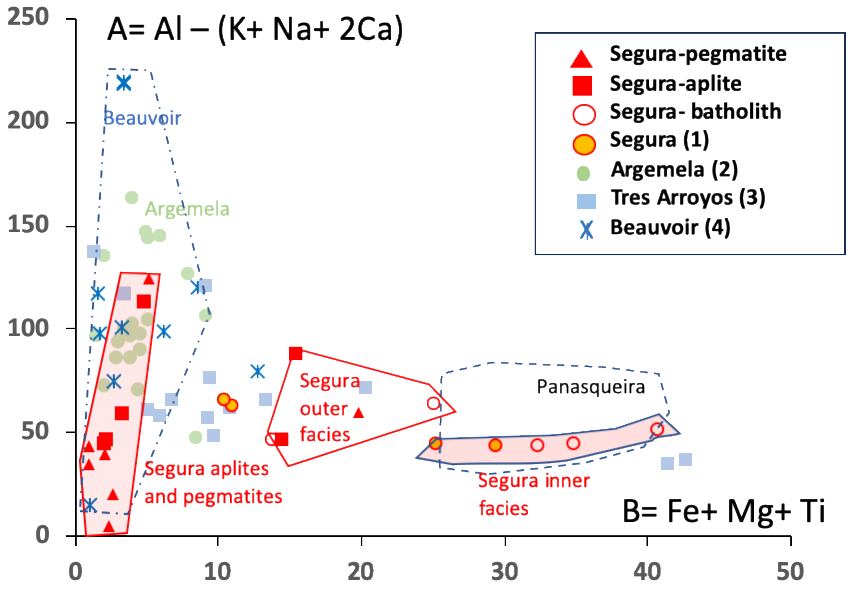

Figure 10. Diagram A (=Al – (K+ Na + Ca)) versus B (=Fe+ Mg+ Mn) from [38] applied to the Segura facies and with a comparison with the reference peraluminous differentiated granites. 1: Segura [5], 2: Argemela [10], 3: Tres Arroyos [3], and 4: Beauvoir [11]. For Panasqueira, only the envelope is shown.

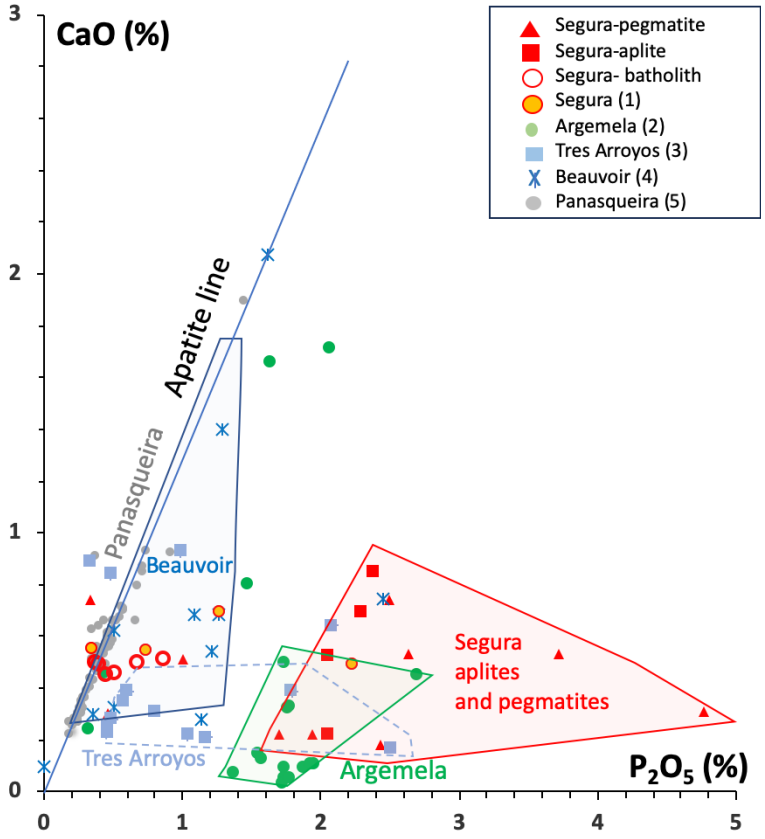

Figure 11. CaO versus P_2O_5 diagram applied to the same series of granites as in Figure 9. It shows the increased phosphorus content of the Segura aplites and pegmatites and the shift from the apatite line, which is high in the Segura and Argemela magmas compared with the other P-rich magmas: 1: Segura [5], 2: Argemela [10], 3: Tres Arroyos [3], 4: Beauvoir [11], and 5: Panasqueira [37].

Thus, data points are located to the right of the apatite line, thereby indicating that for a given calcium content, the phosphorus is connected to another phosphate (Li, Na, or another element such as Sr, for instance, being the dominant phosphate) other than apatite, as confirmed by the petrography and crystal chemistry analyses presented above. The Segura aplites and pegmatites are even more enriched in P_2O_5 than the Argemela granites. The F, Li, and P contents are roughly correlated positively.

5. Discussion

5.1. Comparison with Other Similar Geochemical Suites

Leucocratic peraluminous magmas are formed either by the fractional crystallisation of a parent S-type granitic magma with progressive enrichment in incompatible elements during differentiation [1,3,39] or by anatectic-type melting, which is independent of the formation of the peraluminous granitic plutons that are found in the environment close to pegmatites [4,40]. Low proportions of partial protolith melting could produce low volumes of magmas enriched in incompatible elements, with a mineralogical composition close to the ultimate products of differentiation. This duality between the presence of pegmatites that are often later than the plutons and derived from distinct melting processes at different structural levels in the lithosphere has been evoked in several examples as follows: the Limousin pegmatites (French Massif Central [41]) and the Fregeneda-Almendra pegmatite field in Portugal [42]. The same situation occurs at Segura. The Authors in [5] have already ruled out the hypothesis of a genetic link between the main Cabeza de Araya batholith in Segura and the spatially nearby dykes. What is particularly interesting

here is the extreme enrichment in volatiles (F, Li, and P), which may have also influenced the melting temperature of the magma at the migmatisation front.

The abnormal contents in P, Al, and F are much above those expected from peraluminous granite differentiation [12,43-45]. Figure 12 shows that the Segura aplites and pegmatites have around the same F content as the Argemela and Tres Arroyos granites (2500–4000 ppm) but higher P_2O_5 values between 2 and 3% (Figure 12). The reasons for these high enrichments can differ [46].

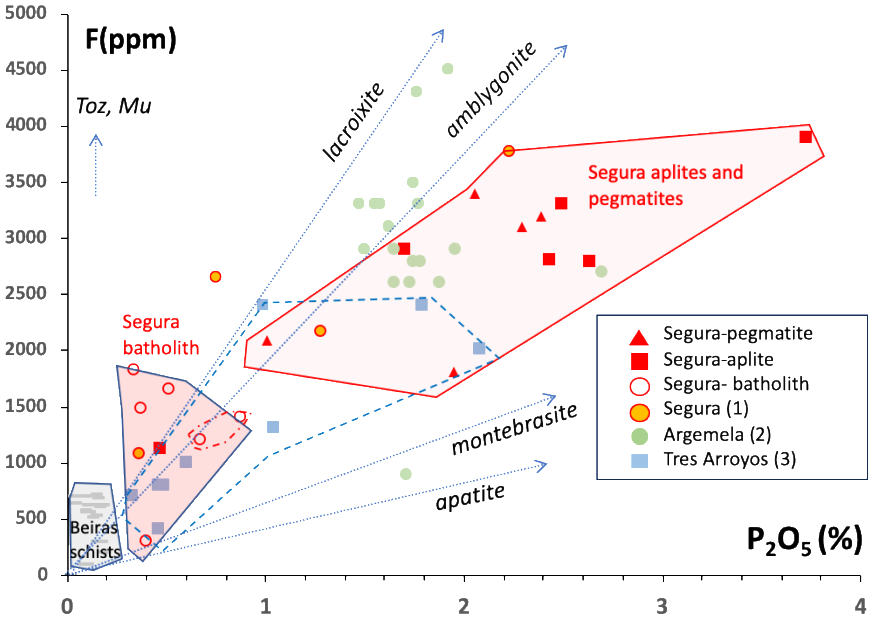

Figure 12. F versus P_2O_5 diagram showing the increased phosphorus content of the Segura aplites and pegmatites (red symbols) as a function of fluorine content. Reference lines in the direction of the phosphate end-members are reported. 1: Segura: [5], 2: Argemela [10], and 3: Tres Arroyos [3].

The studied aplites and pegmatites are particularly enriched in P, F, Li (locally B), Al, and Na and present a positive correlation between all these elements and the aluminium saturation index of ASI = [Al/(Ca − 1.67P + Na + K)] as defined by [47,48] (Figure 13). These enrichments can occur at several stages of the magma genesis, migration, and evolution as follows: from the melting zone, during the upward journey and magmatic differentiation, later when a supercritical fluid is extracted from the cooling magma, and, finally, in the fluid phase acting throughout the magmatic–hydrothermal transition.

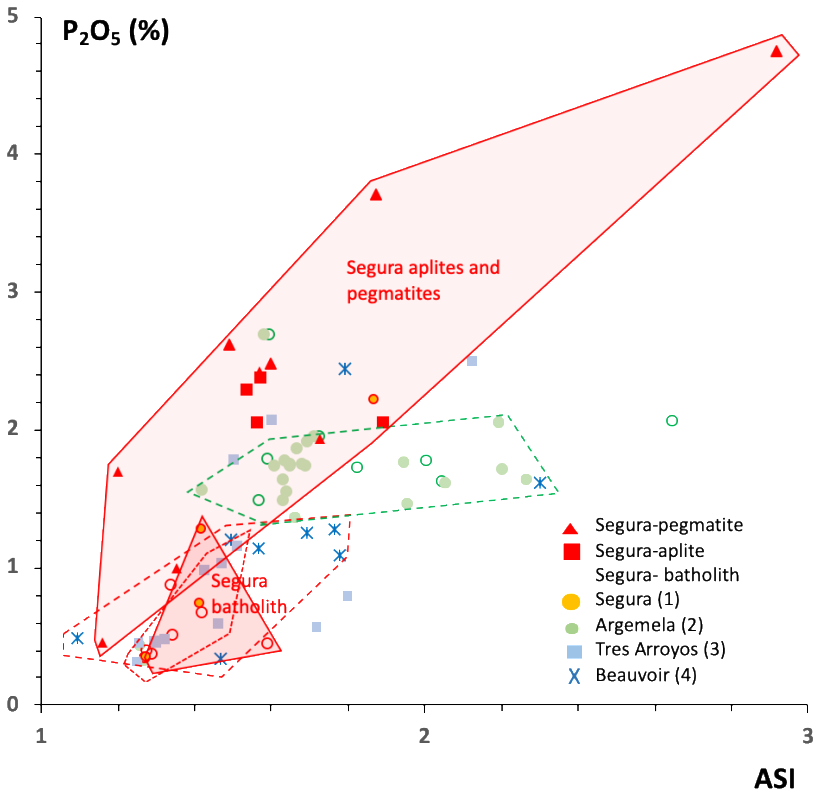

Figure 13. P_2O_5 versus the aluminium saturation index (ASI = [Al/(Ca − 1.67P + Na + K)]) diagram. 1: Segura [5], 2: Argemela [10], 3: Tres Arroyos [3], and 4: Beauvoir [11].

5.2. Causes of Enrichments in Phosphorus, Lithium, and Fluorine

It is difficult to prove that the schists of the Beiras Group, which are the host rocks of the aplite and pegmatite sills, are also the initial sources of the magma. However, the metasedimentary sequence is thick (up to 11 km; [49]) and voluminous, so the melting of metasediments that are compositionally similar to those exposed could be envisaged at a lower level. The P_2O_5, F, and Li content ranges of the Beiras schists are 2000–3000 ppm, 500–700 ppm, and 45–80 ppm, respectively. The F and P_2O_5 concentration ranges in the schists are around two to three times lower than the main batholith granites and five times lower than the outer facies (muscovite granite).

During metapelite anatexis, the phosphorus content of the initial magma is mainly controlled by the apatite content of the source, the degree of melting, and the solubility of the apatite in the melt. The low initial stock of REE and Y explains the absence of monazite or xenotime.

Thomas et al. [50] suggest extreme phosphorus enrichment may be due to metastable sub-liquidus immiscibility. The spontaneous separation into two undercooled melt phases could be linked to thermal fluctuations. Thomas et al. [50] point out that the driving force behind phase separation is a decrease in the free energy of the system.

The very high fluorine content of late-phase liquids could be interpreted as the result of extreme fractionation of granitic magma. The initial content of the parent granitic magma could well be no more than a conventional value of around 0.5–1% F. For phosphorus, Thomas et al. [50] also consider the effect of boiling to be related to decompression after fracturing under the impact of tectonic stress on the formation of phosphorus-enriched globules, which might produce a highly phosphate-rich magma.

5.3. Migration and Extraction of Phosphorus-Rich Magma

The enrichment factor for P_2O_5 is around 2.5 to 3 between the outer muscovite granite and the aplite–pegmatite dykes from Segura and 1.5 to 3 for fluorine concerning the very same group of rocks (Figure 12). The very high levels of F, P, H_2O Li_2O, Rb_2O, Cs_2O, and B in the residual magma liquids related to these rocks may have resulted in a considerable decrease in viscosity, with values of the order of 10 Pa [51,52] and lower being likely. Thanks to this very low viscosity, intergranular magmas can move through granitic matrices according to the model developed by [53]. They can then extract themselves from the magmas and migrate through structural discontinuities (such as shear or fault zones), particularly in the schistose host rock. Such a geometry is typically observed at Segura, i.e., a series of low-dipping dykes filling dilating spaces in the foliation plane or inserting themselves into fractures sub-perpendicular to the foliation, which constitute the most common plane of weakness in the shales.

5.4. The Behaviour of Li, F, and P during the Crystallization of Perphosphorus Magmas

Some phosphorus may be incorporated in crystallising feldspars when calcium is low in the melt. As phosphorus and aluminium form a coupled substitution (the so-called berlinite substitution, $P^{5+} + Al^{3+} = 2Si^{4+}$), the incorporation of phosphorus in feldspar is favoured in peraluminous magmas. Then, considering the strong affinity between P and Li, the phosphorus concentrated in the residual melt is partially removed first by the amblygonite–montebrasite and the eosphorite–childrenite phosphate series formation, which appears first. Amblygonite and eosphorite develop early during the crystallisation of aplites and pegmatites but represent the final stage of the magmatic evolution that began lower down during the crystallisation of the muscovite-rich granite or another non-exposed late intrusive granite. It is difficult to ascribe the Fe-Mn compositional changes to a particular stage of the magma evolution except for its very late crystallisation and a rather low fO_2, allowing for the incorporation of the relatively low amount of iron available in the melt as Fe^{2+} in the eosphorite. At that stage, the crystallisation of the amblygonite–montebrasite series regulates or decreases the fluorine content in the melt [54] and probably the saturation with respect to topaz. During the final stage of the hydrothermal evolution of pegmatites, phosphates from the goyazite–crandallite series form along grain boundaries at the expense of the Li-Na phosphates, after which numerous secondary apatite crystals form and constitute the final expression of the P-bearing phases. When alkali feldspars crystallise out of a perphosphorus and peraluminous magmatic system, they can become the main reservoirs of phosphorus. In the case of Segura, the late apatite grains likely crystallised from this stock, which means that the P concentrations of the feldspars can no longer be used as indicators of the initial P richness of the magma. The overall paragenetic sequence is proposed in Figure 14. According to [55,56], phosphorous can be released secondarily by the Al-Si ordering of alkali feldspars, and fluorine is still high, probably in the remaining fluids. During the magmatic–hydrothermal transition, the crystallisation of these late phosphates needs external hydrothermal inputs (Ca-Sr (Ba), then Ca).

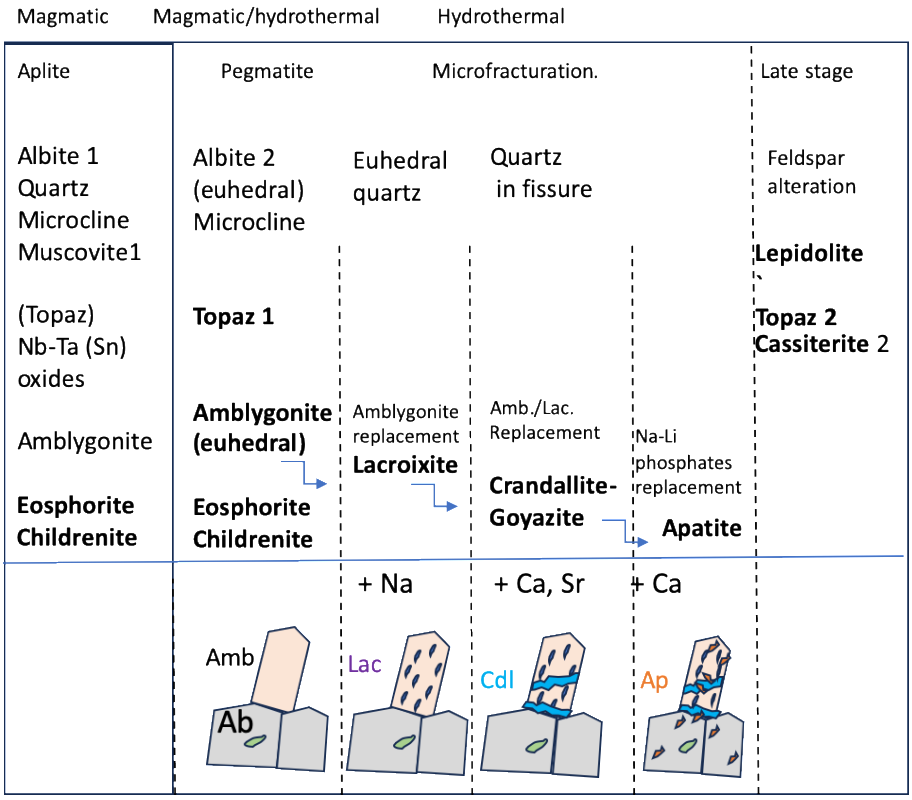

Figure 14. Schematic representation of the mineralogical evolution of the Segura aplites and pegmatites with the time from the magmatic to hydrothermal stages, especially for the phosphates. Amb: amblygonite, Lac: lacroixite, Cdl: crandallite, and Ap: Apatite.

5.5. Conceptual Model of the Melt Injection in the Beiras Schists

A model is proposed for the formation of the aplite–pegmatite dykes at Segura in Figure 15. These dykes cannot be related geochemically to the main inner Cabeza de Araya cordierite monzogranite but only to the external facies, in particular, the muscovite-rich facies, which constitutes a relatively small mass of magmas injected at the boundary between the batholith and the metasedimentary country rocks. The upwelling geometry of the magma that formed the muscovite-rich granite is likely to be independent of that of the main batholith, the centre of which is located more than 40 km to the southeast. As shown by the arrows in Figure 15, the migration pathways are challenging to assess. A fourth magma injection at the boundary with the Cabeza de Araya batholith or a distinct pathway for the muscovite granite could have occurred. The magmas that evolved in the late stages of the Late Variscan evolution appear to have risen through zones of crustal weakness in many places, which could be the case for the Cabeza de Araya batholith [6,30]. In the schematic cross-section of the upper lithosphere thought to represent the situation during the 310–300 Ma period, it is proposed that of a series of intrusive facies ascend from a migmatitic zone at depth. Such a geometry was already suggested by [57] for the G2-G5 including the rare metal granite intrusions at Panasqueira, and the Argemela region (cross-section in [10]) where processes occur under a NE-SW shortening. To explain the formation of dykes in the metasediments near this injection locus, it is once again necessary to refer to the opening conditions of the foliation planes or fractures perpendicular to this plane. The local stress tensor at that time stimulates these openings.

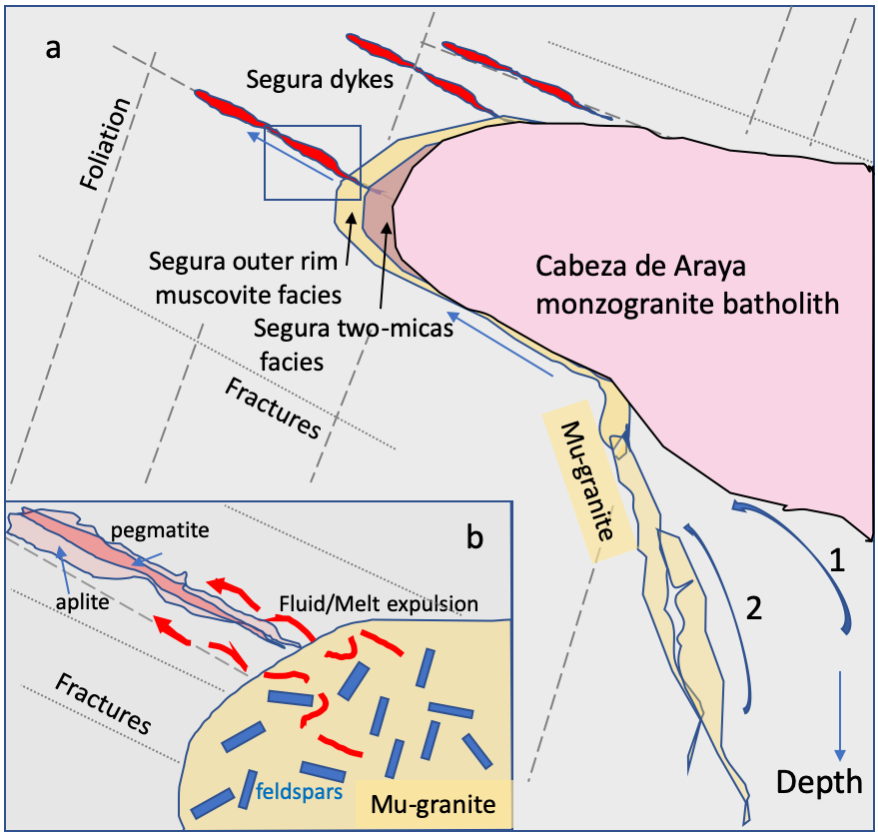

Figure 15. (**a**) Conceptual model of the intrusive dykes (vertical cross-section) in the westernmost sector of the Cabeza de Araya batholith, the intrusion of the muscovite-rich outer facies and dykes in the metasediments. The magma migration pathways are as follows: arrow 1 corresponds to an additional layer of the Cabeza de Araya batholith like the other facies that compose it, with a feeder zone whose centre is located far to the southeast, and arrow 2 to an autonomous magma intrusion that is independent of the initial pathways. (**b**) Inset in figure (**a**), with the extraction of a low-viscosity magma migrating through open tension gashes and fractures in the metasediments.

The formation of magmas hyper-enriched in F, Li, and P was facilitated by the already high concentrations of the muscovite granite facies. Additional processes are required as outlined above, notably filter-pressing mechanisms expulsing these magmas with high water, F, Li, and P contents, and very low viscosity, with these facilitating their extraction from the crystallizing melt when subjected to lateral pressure. Once they have removed themselves from the initial partly crystallised melt, they may migrate into the zones of weakness open in the metasedimentary series. The crystallisation of the aplites and then the pegmatites take place in a sub-closed system. Still, the rise in temperature at the same time triggers convective processes which favour the arrival of fluids in equilibrium with the metamorphic series and induce the elements necessary for the metasomatism of the initial assemblages and, in particular, the crystallisation of the crandallite–goyazite series and the late hydrous apatites. The percolation of late fluids with an essentially metamorphic signature, which is mainly shown by the abundance of methane-rich fluid inclusions, has been identified [58,59]. Unfortunately, this fluid event provoked quartz recrystallisation and has erased all traces of previous magmatic fluids.

6. Conclusions

The aplites and pegmatites of Segura were formed from magma and fluids particularly enriched in phosphorus, fluorine, water, and lithium. Compared with other highly evolved granites, such as those of Argemela, Tres Arroyos, and Beauvoir, the concentrations of P, F, and Li in the aplites and pegmatites are higher than those in the other granites mentioned. Their aluminium saturation index (ASI) is also higher.

The enrichment factors for these elements compared with peraluminous granites or monzogranites are 1.5 to 5. These enrichments were made possible by favourable processes such as extracting the low-viscosity magma from the crystallizing melt.

The formation of the dykes in the metasediments took place close to the main injection site of the muscovite-rich granite, which is off-centre from that of the Cabeza de Araya monzogranite. The opening of the foliation planes or fractures perpendicular to this plane required sub-horizontal stresses during a major compression event linked to the opening of the main muscovite granite feeder drain from the deep zones where the partial melting of the metasediments occurs.

The paragenetic sequences were demonstrated using micro-X-ray fluorescence chemical imaging and show the phosphates crystallise to be in the following order: Fe-Mn phosphate > amblygonite (montebrasite) > lacroixite > crandallite–goyazite > apatite-Mn. The alteration of the initial lithium-bearing phosphate assemblage is consistent with developments already described elsewhere, notably that of the crystallisation of lacroixite at the expense of amblygonite, the formation of the crandallite–goyazite series at the expense of amblygonite, and hydrothermal apatite at the expense of albite and the earlier phosphate phases.

The contribution of calcium and other divalent cations indicates the late involvement of hydrothermal fluids external to the magmatic system.

Author Contributions: M.C., sampling, data acquisition and interpretation, conceptualization, writing (original draft preparation, review and editing), and funding acquisition; M-C B.., sampling, data acquisition and interpretation, writing (review and editing), and funding acquisition; A.L., data acquisition and writing (review and editing); I.M., fieldwork, geological mapping, sampling, and writing (review and editing); Í.D.S., fieldwork, geological mapping, sampling, and writing (review and editing); A.M., fieldwork, geological mapping, sampling, conceptualization, data interpretation, writing (review and editing), and funding acquisition. All authors have read and agreed to the published version of the manuscript.

Funding: This research was funded by ERAMIN2 through the project MOSTMEG (n°: ERA-MIN/0002/2019 (for more details: http://doi.org/10.54499/ERA-MIN/0002/2019; https://mostmeg.rd.ciencias.ulisboa.pt/). This work contributes to a better knowledge of granite-related ore systems, namely those enriched in lithium. It benefits the research carried out within the framework of the programmes of Labex Ressources21 under the reference ANR-10-LABX-21-RESSOURCES21 supported by the Agence Nationale de la Recherche through the national programme "Investissements d'avenir", which contributes to the co-funding of the ERAMIN project. Additional support came from the Portuguese Fundação para a Ciência e a Tecnologia (F.C.T.) I.P./MCTES through the PIDDAC national funds (n°s: UIDB/50019/2020, LA/P/0068/2020; more details at https://doi.org/10.54499/UIDB/50019/2020; https://doi.org/10.54499/LA/P/0068/2020) and PD/BD/142783/2018).

Data Availability Statement: The data presented in this study are available on request from the corresponding author due to the future reseach data based.

Acknowledgments: O. Rouer and M.C. Caumon (GeoRessources) are thanked for their help when acquiring the EMPA and Raman data. Four anonymous reviewers are warmly acknowledged for their suggestions.

Conflicts of Interest: The authors declare no conflicts of interest.

References

1. Breiter, K.; Durisova, J.; Korbelova, Z.; Lima, A.; Vasinova Galiova, M.; Hlozkova, M.; Dosbaba, M. Rock textures and mineral zoning—A clue to understanding rare-metal granite evolution: Argemela stock, Central-Eastern Portugal. *Lithos* **2022**, *410–411*, 106562.
2. Garate-Olave, I.; Müller, A.; Roda-Robles, E.; Gil-Crespo, P.P.; Pesquera, A. Extreme fractionation in a granite–pegmatite system documented by quartz chemistry: The case study of Tres Arroyos (Central Iberian Zone, Spain). *Lithos* **2017**, *286*, 162–164.
3. Garate-Olave, I.; Roda-Robles, E.; Gil-Crespo, P.P.; Pesquera, A.; Errandonea-Martin, J. The Tres Arroyos granitic aplite-pegmatite field (Central Iberian Zone, Spain): Petrogenetic constraints from the evolution of Nb-Ta-Sn oxides, whole-rock geochemistry and U-Pb geochronology. *Minerals* **2020**, *10*, 1008.

4. Webber, K.L.; Simmons, W.B.; Falster, A.U.; Hanson, S.L. Anatectic pegmatites of the Oxford County pegmatite field, Maine, USA. *Can. Mineral.* **2019**, *57*, 811–815.
5. Antunes, I.M..; Neiva, A.M.; Farinha Ramos, J.M.; Silva, P.B.; Silva, M.M.; Corfu, F. Petrogenetic links between lepidolite-subtype aplite-pegmatite, aplite veins and associated granites at Segura (central Portugal). *Chem. Erde Geochem*. **2013**, *73*, 323–341.
6. Castro, A. Structural pattern and ascent model in the Central Extremadura batholith, Hercynian belt, Spain. *J. Struct. Geol.* **1986**, *8*, 633–645.
7. Corretgé, L.G.; Suarez, O. A Garnet-Cordierite Granite Porphyry Containing Rapakivi Feldspars in the Cabeza de Araya Batholith (Extremadura, Spanish Hercynian Belt). *Mineral. Petrol.* **1994**, *50*, 97–111.
8. Fernandéz, C.; Castro, A. Pluton accommodation at high strain rates in the upper continental crust. The example of the Central Extremadura batholith, Spain. *J. Structural Geol*. **1999**, *21*, 1143–1149.
9. García-Moreno, O.; Corretgé, L.G.; Holtz, F.; García-Aria, M.; Rodríguez, C. Phase relations in the Cabeza de Araya cordierite monzogranite, Iberian Massif: Implications for the formation of cordierite in a crystal mush. *Geol. Acta* **2017**, *15*, 337–359.
10. Michaud, J.A.S.; Gumiaux, C.; Pichavant, M.; Gloaguen, E.; Marcoux, E. From magmatic to hydrothermal Sn-Li-(Nb-Ta-W) mineralization: The Argemela area (central Portugal). *Ore Geol. Rev*. **2020**, *116*, 103215.
11. Cuney, M.; Marignac, C.; Weisbrod, A. The Beauvoir topaz-lepidolite albite granite (Massif Central, France)—The disseminated magmatic Sn-Li-Ta-Nb-Be mineralization. *Econ Geol.* **1992**, *87*, 1766–1794.
12. London, D.; Wolf, M.B.; Morgan, G.B.; Gallego-Garrido, M. Experimental Silicate–Phosphate Equilibria in Peraluminous Granitic Magmas, with a Case Study of the Alburquerque Batholith at Tres Arroyos, Badajoz, Spain. *J. Petrol*. **1999**, *40*, 215–240.
13. Garate-Olave, I.; Roda-Robles, E.; Gil-Crespo, P.P.; Pesquera, A. The phosphate mineral associations from the Tres Arroyos aplite-pegmatites (Badajoz, Spain): Petrography, mineral chemistry and petrogenetic implications. *Can. Mineral.* **2020**, *58*, 747–765.
14. Ribeiro, A.; Munhá, J.; Dias, R.; Mateus, A.; Pereira, E.; Ribeiro, L.; Fonseca, P.; Araújo, A.; Oliveira, T.; Romão, J.; et al. Geodynamic evolution of the SW Europe Variscides. *Tectonics* **2007**, *26*, TC6009.
15. Díez Fernández, R.; Pereira, M.F. Extensional orogenic collapse captured by strike-slip tectonics: Constraints from structural geology and U-Pb geochronology of the Pinhel shear zone (Variscan orogen, Iberian Massif). *Tectonophysics* **2016**, *691*, 290–310.
16. Azor, A.; Dias da Silva, Í.; Gómez Barreiro, J.; González-Clavijo, E.; Martínez Catalán, J.R.; Simancas, J.F.; Martínez Poyatos, D.; Pérez-Cáceres, I.; González Lodeiro, F.; Expósito, I.; et al. Deformation and Structure. In *The Geology of Iberia: A Geodynamic Approach: Volume 2: The Variscan Cycle*; Quesada, C., Oliveira, J.T., Eds.; Springer International Publishing: Cham, Switzerland, 2019; pp. 307–348.
17. Dias da Silva, Í.; González Clavijo, E.; Díez-Montes, A. The collapse of the Variscan belt: A Variscan lateral extrusion thin-skinned structure in NW Iberia. *Int. Geol. Rev.* **2021**, *63*, 659–695.
18. Dias da Silva, I.; Gomez-Barreiro, J.; Martínez Catalan, J.R.; Ayarza, P.; Pohl, J.; Martinez, E. Structural and microstructural analysis of the Retortillo Syncline (Variscan belt, Central Iberia). Implications for the Central Iberian Orocline. *Tectonophysics* **2017**, *717*, 99–115.
19. Ribeiro, M.L.; Castro, A.; Almeida, A.; González Menéndez, L.; Jesus, A.; Lains, J.A.; Lopes, J.C.; Martins, H.C.B.; Mata, J.; Mateus, A.; et al. Variscan Magmatism. In *The Geology of Iberia: A Geodynamic Approach, Regional Geology Reviews*; Quesada, C., Oliveira, J.T., Eds.; Springer, Cham, Switzerland, 2019.
20. Villaseca, C.; Barbero, L.; Herreros, V. A re-examination of the typology of peraluminous granite types in intracontinental orogenic belts. *Trans. R. Soc. Edinb. Earth Sci.* **1998**, *89*, 113–119.
21. Dias, G.; Leterrier, J.; Mendes, A.; Simoes, P.P.; Bertrand, J.M. U–Pb zircon and monazite geochronology of post-collisional Hercynian granitoids from the Central Iberian Zone (Northern Portugal). *Lithos* **1998**, *45*, 349–369.
22. Lopez Plaza, M.Y.; Martinez Catalan, J.R. Síntesis estructural de los granitoides hercínicos del Macizo Hespérico. In *Geología de los Granitoides y Rocas Asociadas del Macizo Hespérico*; Bea, F., Carnicero, A., Gonzalo, J.C., Lopez Plaza, M., Rodriguez Alonso, M.D., Eds.; Libro homenaje a L.C. García de Figuerola: Editorial Rueda, Madrid, 1987, pp. 195–210.
23. Roda-Robles, E.; Villaseca, C.; Pesquera, A.; Gil-Crespo, P.P.; Vieira, R.; Lima, A.; Garate-Olave, I. Petrogenetic relationships between Variscan granitoids and Li-(F-P)-rich aplite-pegmatites in the Central Iberian Zone: Geological and geochemical constraints and implications for other regions from the European Variscides. *Ore Geol. Rev.* **2018**, *95*, 408–430.
24. Martins, I.; Mateus, A.; Cathelineau, M.; Boiron, M.C.; Ribeiro da Costa, I.; Dias da Silva, Í.; Gaspar, M. The Lanthanide "Tetrad Effect" as an Exploration Tool for Granite-Related Rare Metal Ore Systems: Examples from the Iberian Variscan Belt. *Minerals* **2022**, *12*, 1067.
25. Melleton, J.; Gloaguen, E.; Frei, D.; Lima, A.; Vieira, R.; Martins, T. Polyphased rare-element magmatism during late orogenic evolution: Geochronological constraints from NW Variscan Iberia. *Bull. Soc. Geol. Fr*. **2022**, *193*, 7.
26. Pereira, A.; Pereira, L.; Macedo, C. Os plutonitos da Zebreira (Castelo Branco): Idade e enquadramento estructural. *Mem. Not. Publ. Mus. Lab. Mineral. Geol.* **1986**, *101*, 21–31.
27. Antunes, I.M.; Neiva, A.M.; Silva, M.M.; Corfu, F. The genesis of I- and S-type granitoid rocks of the Early Ordovician Oledo pluton, Central Iberian Zone (central Portugal). *Lithos* **2009**, *111*, 168–185.
28. Inverno, C.; Carvalho, D.d.; Parra, A.; Reynaud, R.; Filipe, A.; Martins, L. *Carta de Depósitos Minerais de Portugal (Folha 3), à Escala 1:200,000*; LNEG: Lisboa, Portugal, 2020.

29. Instituto Geológico e Mineiro, Carta Geológica de Portugal, escala 1:500.000. Serviços Geológicos de Portugal, Instituto Geológico e Mineiro, 1992.
30. Vigneresse, J.L.; Bouchez, J.L. Successive granitic magma batches during pluton emplacement: The case of Cabeza de Araya (Spain). *J. Petrol*. **1997**, *38*, 1767–1776.
31. Sousa, M.B. Considerações sobre a estratigrafia do Complexo Xisto-Grauváquico (CXG) e sua relação com o Paleozóico Inferior. *Cuad. Geol. Ibérica* **1984**, *9*, 9–36.
32. Carignan, J.; Hild, P.; Mevelle, G.; Morel, J.; Yeghicheyan, D. Routine analyses of trace elements in geological samples using flow injection and low pressure on line liquid chromatography coupled to ICP-MS: A study of geochemical reference material B.R., DR-N, EB-N, AN-G and G.H. *Geostand. Newsl.* **2001**, *25*, 187–198.
33. Lafuente, B.; Downs, R.T.; Yang, H.; Stone, N. The power of databases: The RRUFF project. In *Highlights in Mineralogical Crystallography*; Armbruster, T., Danisi, R.M., Eds.; W. De Gruyter: Berlin, Germany, 2015; pp. 1–30.
34. Frost, R.L.; Xi, Y.; Scholz, R.; López, A.; Lima, R.M.F.; Ferreira, C.M. Vibrational spectroscopic characterization of the phosphate mineral series eosphorite–childrenite–(Mn,Fe)Al(PO_4)$(OH)_2$·(H_2O) *Vib. Spectr.* **2013**, *67*, 4–21.
35. Rondeau, B.; Fritsch, E.; Lefèvre, P.; Guiraud, M.; Fransolet, A.-M.; Lulzac, Y. A Raman investigation of the amblygonite-montebrasite series. *Can. Mineral*. **2006**, *44*, 1109–1117.
36. Cerný, P.; Ercit, T.S. Mineralogy of niobium and tantalum: Crystal chemistry relationship, paragenetic aspects and their economic implications. In *Lanthanides, Tantalum and Niobium*; Moller, P., Černý, P., Saupé, F., Eds.; Springer: Berlin, Germany, 1989; pp. 27–29.
37. Marignac, C.; Cuney, M.; Cathelineau, M.; Lecomte, A.; Carocci, E.; Pinto, F. The Panasqueira rare metal granite suites and their involvement in the genesis of the world-class Panasqueira W–Sn–Cu vein deposit: A petrographic, mineralogical, and geochemical study. *Minerals* **2020**, *10*, 562.
38. Debon, F.; Lefort, P. A cationic classification of common plutonic rocks and their magmatic associations: Principles, method, applications. *Bul. Min*. **1988**, *111*, 493–510.
39. Cerny, P. Geochemical and Petrogenetic Features of Mineralization in Rare Element Granitic Pegmatites in the Light of Current Research. *Appl. Geochem*. **1992**, *7*, 393–416.
40. Simmons, W.; Falster, A.; Webber, K.; Roda-Robles, E. Bulk composition of mt. Mica pegmatite, Maine, USA: Implications for the origin of an L.C.T. type pegmatite by anatexis. *Can. Mineral*. **2016**, *54*, 1053–1070.
41. Deveaud, S.; Gumiaux, C.; Gloaguen, E.; Branquet, Y. Spatial statistical analysis applied to rare-element LCT-type pegmatite fields: An original approach to constrain faults-pegmatites-granites relationships. *J Geosci*. **2013**, *58*, 163–182.
42. Roda-Robles, E.; Vieira, R.; Lima, A.; Errandonea-Martin, J.; Pesquera, A.; Cardoso-Fernandes, J.; Garate-Olave, I. Li-rich pegmatites and related peraluminous granites of the Fregeneda-Almendra field (Spain-Portugal): A case study of magmatic signature for Li enrichment. *Lithos* **2023**, *452–453*, 107195.
43. Pichavant, M. Experimental Crystallization of the Beauvoir Granite as a Model for the Evolution of Variscan Rare Metal Magmas. *J. Petrol*. **2022**, *63*, egac120.
44. London, D. Phosphorus in S-type magmas: The P_2O_5 content of feldspars from granites, pegmatites, and rhyolites. *Amer. Mineral.* **1992**, *77*, 126–145.
45. London, D.; Morgan VI, G.B.; Babb, H.A.; Loomis, J.L. Behavior and effects of phosphorus in the system Na_2O–K_2O–Al_2O_3–SiO_2–P_2O_5–H_2O at 200 MPa. *Contrib. Mineral. Petrol.* **1993**, *113*, 450–465.
46. Bea, F.; Fershtater, G.B.; Corretge, L.G. The geochemistry of phosphorus in granite rocks and the effect of aluminium. Lithos 1992, 29, 43–56.
47. Shand, S.J. The Eruptive Rocks, 2nd ed.; John and Wiley Sons: New York, NY, USA, 1943; 444p.
48. Frost, B.R.; Barnes, C.G.; Collins, W.J.; Arculus, R.J.; Ellis, D.J.; Frost, C.D. A Geochemical Classification for Granitic Rocks. J. Petrol. 2001, 42, 2033–2048.
49. Villaseca, C.; Merino, E.; Oyarzun, R.; Orejana, D.; Pérez-Soba, C.; Chicharro, E. Contrasting chemical and isotopic signatures from Neoproterozoic metasedimentary rocks in the Central Iberian Zone (Spain) of pre-Variscan Europe: Implications for terrane analysis and Early Ordovician magmatic belts. *Precambrian Res.* **2014**, *245*, 131–145.
50. Thomas, R.; Webster, J.D.; Rhede, D. Strong phosphorus enrichment in a pegmatite-forming melt. Acta Universitatis Carolinae. *Geologica* **1998**, *42*, 150–164.
51. Thomas, R.; Rhede, D.; Trumbull, R.B. Microthermometry of volatile-rich silicate melt inclusions in granitic rocks. *Z. Geol. Wiss.* **1996**, *24*, 505–526.
52. Webster, J.D.; Thomas, R.; Rhede, D.; Forster, H.J.; Seltmann, R. Melt inclusions in quartz from an evolved peraluminous pegmatite: Geochemical evidence for strong tin enrichment in fluorine-rich and phosphorus-rich residual liquids. *Geochim. Cosmochim. Acta* **1997**, *61*, 2589–2604.
53. Harte, B.; Hunter, R.H.; Kinny, P.D. Melt geometry, movement and crystallization, in relation to mantle dykes, veins and metasomatism. *Trans. R. Soc. London* **1993**, *342*, 1–21.
54. London, D.; Morgan VI, G.B.; Wolf, M.B. Amblygonite-montebrasite solid solutions as monitors of fluorine in evolved granitic and pegmatitic melts. *Am. Mineral.* **2001**, *86*, 225–233.

55. Frýda, J.; Breiter, K. Alkali feldspars as a main phosphorus reservoir in rare-metal granites: Three examples from the Bohemian Massif (Czech Republic). *Terra Nova,* **1995**, *7*, 315–320.
56. Kontak, D.J.; Martin, R.F.; Richard, L. Patterns of phosphorus enrichment in alkali feldspar, South Mountain Batholith, Nova Scotia, Canada. *Eur. J. Miner*. **1996**, *8*, 805–824.
57. Cathelineau, M.; Boiron, M.-C.; Marignac, C.; Dour, M.; Dejean, M.; Carocci, E.; Truche, L.; Pinto, F. High pressure and temperatures during the early stages of tungsten deposition at Panasqueira revealed by fluid inclusions in topaz. *Ore Geol. Rev.* **2020**, *126*, 103741.
58. Yakovenko, A. Estudo de Inclusões Fluidas Dos filões Pegmatíticos Litiníferos de Segura. Master Thesis, Porto University, Porto, Portugal, 2021; 107p.
59. Yakovenko, A.; Guedes, A.; Boiron, M.C.; Cathelineau, M.; Martins, I.; Mateus, A. Fluid inclusion studies in quartz from the Li-rich pegmatite veins from Segura. In *Proc. Jornadas do ICT*, Evora, Portugal, ICT, Evora-Porto, Portugal, ISBN: 978-972-778-232-1, 2022; p. 43.